Quantum Dot-Based Frequency Multiplier

G.A. Oakes,[1,2,†] L. Peri,[1,2,†] L. Cochrane,[1,2] F. Martins,[3] L. Hutin,[4] B. Bertrand,[4] M. Vinet,[4]
A. Gomez Saiz,[2] C.J.B. Ford,[1] C.G. Smith,[1,3] and M.F. Gonzalez-Zalba[2,*]

[1] *Cavendish Laboratory, University of Cambridge, J. J. Thomson Avenue, Cambridge CB3 0HE, United Kingdom*
[2] *Quantum Motion, 9 Sterling Way, London N7 9HJ, United Kingdom*
[3] *Hitachi Cambridge Laboratory, J. J. Thomson Avenue, Cambridge CB3 0HE, United Kingdom*
[4] *Laboratoire d'électronique des technologies de l'information (CEA-Leti), Minatec Campus, Grenoble F-38054, France*

(Received 28 November 2022; revised 27 February 2023; accepted 16 May 2023; published 20 June 2023)

Silicon offers the enticing opportunity to integrate hybrid quantum-classical computing systems on a single platform. For qubit control and readout, high-frequency signals are required. Therefore, devices that can facilitate its generation are needed. Here, we present a quantum dot-based radio-frequency multiplier operated at cryogenic temperatures. The device is based on the nonlinear capacitance-voltage characteristics of quantum dot systems arising from their low-dimensional density of states. We implement the multiplier in a multigate silicon-nanowire transistor using two complementary device configurations: a single quantum dot coupled to a charge reservoir and a coupled double quantum dot. We study the harmonic voltage conversion as a function of the energy detuning, the multiplication factor, and the harmonic phase noise and find near ideal performance up to a multiplication factor of 10. Our results demonstrate a method for high-frequency conversion that could be readily integrated into silicon-based quantum computing systems and be applied to other semiconductors.

DOI: 10.1103/PRXQuantum.4.020346

I. INTRODUCTION

Quantum dots (QDs) show great promise as a scalable platform for quantum computation [1], following the recent demonstrations of universal control of four- and six-qubit systems [2,3] and the scaling to 4 × 4 QD arrays [4]. QDs in silicon as a host for spin qubits are particularly attractive due to the demonstrated high-fidelity control [5–7], industrial manufacturability [8,9], and cointegration with classical cryogenic electronics [10–12] and the availability of detailed proposals for large-scale integration [13–19].

As QDs become an established platform for qubit implementation, novel ways of operating such devices are beginning to emerge, providing an opportunity to integrate on the same embodiment additional functionalities. In particular, by exploiting the nonlinear high-frequency admittance, QDs can be utilized as compact charge sensors [20,21], fast local thermometers [22,23], or as parametric amplifiers [24] for quantum-limited amplification. Here, we present a new functional implementation: a QD-based radio-frequency (rf) multiplier.

A frequency multiplier typically consists of a nonlinear circuit element that distorts a sinusoidal signal, generating multiple harmonics. A band-pass filter is then used to select a particular harmonic. Commercially, this can be achieved by utilizing, e.g., semiconductor-based diodes or amplifiers but these dissipate energy reducing their power-conversion performance. Alternatively, microelectromechanical resonators can be utilized for multiplication with enhanced performance due to their low-loss nature [25].

In this paper, we propose and demonstrate a QD-based radio-frequency multiplier in silicon. We demonstrate frequency multiplication on a single device in two complementary configurations: a single QD coupled to a reservoir and a double QD. Due to the nondissipative nature of the device impedance under elastic tunneling conditions, the devices show near-ideal power conversion and phase-noise properties for a multiplication factor of up to 10. Such devices could be utilized to alleviate the challenges associated with the delivery of high-frequency signals to quantum processors from room temperature down to cryogenic stages in dilution refrigerators while reducing

---

[*] fernando@quantummotion.tech

[†] These authors contributed equally to this work.

Published by the American Physical Society under the terms of the Creative Commons Attribution 4.0 International license. Further distribution of this work must maintain attribution to the author(s) and the published article's title, journal citation, and DOI.

the cost and complexity of the room-temperature electronics.

II. QD FREQUENCY MULTIPLICATION

The device used to demonstrate frequency multiplication is the same as in Ref. [20]. It consists of a fully depleted silicon-nanowire transistor with four wraparound gates in series, as shown in Fig. 1(a). QDs form under the gates at cryogenic temperatures when biased close to the threshold voltage [26]. In this demonstration, we utilize voltages on gates 1 (V_{g1}) and 2 (V_{g2}) to form either a QD coupled to a reservoir or a double QD. Further, we apply a rf signal via gate 2 and then measure the transmission through the QD system at the output of an *LC* lumped-element resonator connected to gate 1, which acts as a high-quality band-pass filter around its natural frequency, $f_r = 789$ MHz. Changes in transmitted voltage through the setup are directly proportional to the admittance Y of the device and since, in QD systems, the admittance Y is a highly nonlinear function of the gate voltage [27–32], they can be utilized for frequency multiplication when driven beyond QD's linear regime, as we see later.

Throughout the text, we refer to the concept of detuning ε. For a single QD exchanging an electron with a reservoir (dot-to-reservoir, or DTR, transition), this represents the detuning between the QD electrochemical level and the Fermi level at the reservoir. In the case of an interdot charge transition (ICT), it is the energy detuning between QDs that form a tunnel-coupled two-level system. In this work, we focus on the case of time-dependent detuning with a constant dc value and an oscillatory rf component [$\varepsilon(t) = \varepsilon_0 + \delta\varepsilon \cos \omega t$]. These quantities are directly proportional to the gate voltages throughout this work via two lever arms: α_{dc}, which defines the static detuning via ε_0 and α_{rf}, which defines the rf driving of the quantum systems $\delta\varepsilon$. Moreover, we must define a third lever arm, α_c, which represents the relative capacitive coupling to the gate connected to the band-pass filter, through which the gate current is ultimately collected and measured. The relation between these quantities and the more common lever-arm matrix is outside the scope of this work and is instead outlined in Appendix A.

We now explain the nonlinearity of QD systems in detail. The nonlinear admittance arises from the dependence of the gate charge (Q_g) on the gate voltage. More particularly, for a QD coupled to a reservoir in the fast-relaxation regime, $f \ll \Gamma_R$, where Γ_R is the charge tunneling rate, the gate charge reads

$$Q_g = e\alpha_c P(t) = e\alpha_c f\,(\varepsilon(t)) = \frac{e\alpha_c}{\exp[\varepsilon(t)/k_B T] + 1}, \tag{1}$$

where P is the electron-occupation probability, f is the Fermi-Dirac probability distribution, k_B is the Boltzmann constant, e is the charge of an electron, and T is the system temperature. In the case of a double quantum dot (DQD), in the adiabatic limit, the gate charge is

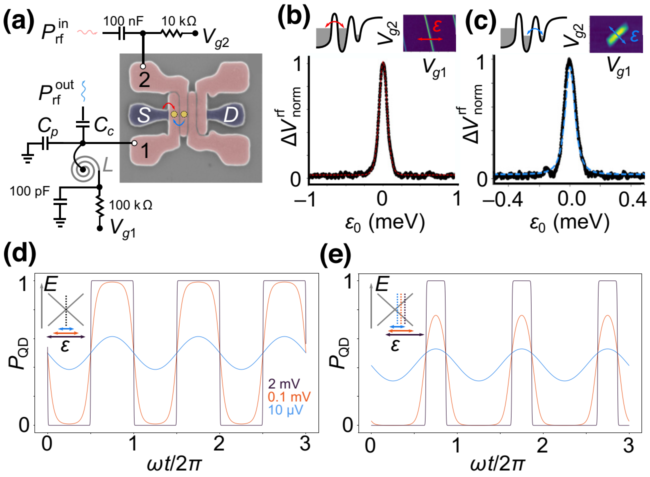

FIG. 1. The device and the experimental setup. (a) A false-colored scanning electron micrograph of a silicon-nanowire transistor with wraparound gates, under which QDs form (yellow circles). An rf signal is applied to gate 2 via a fast line. The signal is measured in transmission from gate 1 via a lumped-element *LC* resonator, which acts as a narrow band-pass filter at f_r. (b),(c) The normalized change in rf voltage due to electron tunneling across a (b) DTR transition and (c) the ICT probed at f_r.The insets in both figures schematically represent the tunneling processes and show the charge-stability maps with the relevant transitions and how detuning ε is defined. (d),(e) Simulations of the electron-occupation probability of a QD for (d) zero and (e) nonzero detuning ε_0 for different driving amplitudes $\delta\varepsilon$. (e) By strongly driving the system, a nonlinear response occurs, tending toward a square, where the duty cycle can be tuned by adjusting $\frac{\varepsilon_0}{\delta\varepsilon}$, which here is set to 75%.

$$Q_g = e\alpha_c P(t) = \frac{e\alpha_c}{2}\left[1 + \frac{\varepsilon(t)}{\sqrt{\varepsilon(t)^2 + \Delta^2}}\right] = \\ = \frac{e\alpha_c}{2}\left[1 + \Pi(t)\right], \tag{2}$$

where in this case $\varepsilon(t)$ refers to the energy detuning between QDs with the corresponding collection lever arm. Besides $\Delta = 2t_c$ is the coupling term, where t_c is the tunnel coupling [30]. When subject to the oscillatory detuning due to the rf excitation, an oscillatory gate current flows through the system proportional to its admittance:

$$I_g = e\alpha_c \frac{dP(t)}{dt} = YV_g. \tag{3}$$

Changes in device admittance occur either due to DTR charge transition, as shown in Fig. 1(b), or ICTs, depicted in Fig. 1(c) with their corresponding fits using the calculated admittance. If the rf excitation is small ($\delta\varepsilon \ll k_B T, \Delta$), the DTR transition or ICT respond linearly to the input voltage. In this regime, the charge oscillates at the rf frequency, with a phase shift dependent on the magnitude of the Sisyphus resistance [31] [see the blue traces in Figs. 1(d) and 1(e)]. When driving the systems beyond their linear regime, the charge distribution gets distorted as the QD is either filled or emptied. As long as $\delta\varepsilon$ remains smaller than the charging energy, the system is required to obey $0 \leq P \leq 1$ at all times. Eventually, in the large-signal regime ($\delta\varepsilon \gg k_B T, \Delta$), $P(t)$ acquires a square-wave-like response containing high-frequency harmonics of the original signal [see Figs. 1(d) and 1(e) and Appendix B]. By comparing Eqs. (1) and (2), we note how in the thermally broadened regime, the DTR transition depends exponentially on ε, while $\Pi(\varepsilon)$ is a polynomial function. If the transitions are lifetime broadened, Eqs. (1) and (2) are convolved with a Lorentzian distribution (see Appendix C). Regardless, we expect the DTR transition to show a higher degree of nonlinearity than the ICT in the intermediate-signal regime, as we see later.

Following the derivation in Appendix C, we can then express the rf-voltage output at the Nth harmonic, $|\Delta V_N^{\text{rf, out}}|$, in terms of the Nth harmonic of the gate current and hence that of the charge occupation probability,

$$|\Delta V_N^{\text{rf, out}}| \propto \left| \int_0^{\frac{2\pi}{N\omega}} e^{iN\omega t} P(t) dt \right| \equiv P_N. \tag{4}$$

For a DTR transition with tunnel rate Γ_R, a simple analytical solution can be found for the output voltage at the Nth harmonic,

$$|\Delta V_N^{\text{rf, out}}| \propto \left| \frac{\Gamma_R}{\Gamma_R + iN\omega} f_N \right|, \tag{5}$$

where we define f_N as

$$f_N = \frac{\omega}{2\pi} \int_0^{\frac{2\pi}{\omega}} e^{iN\omega t} f\,(\varepsilon_0 + \delta\varepsilon \cos \omega t) dt.$$

For the ICT, there is no simple general analytical solution for the output voltage, equivalent to Eq. (4) (see Appendix B). However, using a semiclassical approach, we derive a simple expression for the driven probability distribution. In the regime of fast relaxation, i.e., $\Gamma_P \gg \omega$, where Γ_P is the coupling rate to the phonon bath, absorption and emission mix the ground and excited states, driving them to thermal equilibrium faster than the basis rotation caused by the rf perturbation [31]. If we define $n_0 = b\left(\sqrt{\Delta^2 + \varepsilon_0^2}\right)$, where $b(E) = 1/(e^{E/k_B T} - 1)$ is the Bose-Einstein distribution, we find a simple expression for the driven probability distribution:

$$P(t) = \frac{1}{2} + \frac{1}{2n_0 + 1} \Pi(t). \tag{6}$$

Equation (6) presents the same large-signal square-wave limit discussed thus far but with a different response to the DTR transition in the intermediate regime. We note that the equation is valid in the limit of $\Delta^2 \gg \hbar\omega\delta\varepsilon$, where the evolution can be considered adiabatic.

Finally, we find that in the large-signal regime, ($\delta\varepsilon \gg k_B T, \Delta$), both systems, QD and DQD, produce an output voltage given by

$$|\Delta V_N^{\text{rf, out}}| \propto \frac{1}{N} \sin\left[N \arccos\left(\frac{\varepsilon_0}{\delta\varepsilon}\right)\right], \tag{7}$$

which unifies the large-signal response of the DTR transition and ICT, as it only depends on ε_0 and $\delta\varepsilon$ and not on the physical characteristics of the particular quantum systems. Equation (7) also highlights that the maximum voltage conversion at the Nth harmonic follows a N^{-1} trend, which translates into the maximum N^{-2} trend for the well-known maximum power-conversion efficiency of an ideal frequency multiplier. Further, we note that the detuning offset, ε_0, changes the duty cycle DC of the squarelike output wave (see Appendix B) as we vary the probability of the QD being filled or emptied, as shown in Fig. 1(e). Accordingly,

$$D_c = \frac{1}{\pi} \arccos\left(\frac{\varepsilon_0}{\delta\varepsilon}\right), \tag{8}$$

if $\delta\varepsilon \geq |\varepsilon_0|$, while the QD remains trivially empty or full if $\varepsilon(t)$ never changes sign. The offset detuning dependence of DC, and thus $\Delta V_N^{\text{rf, out}}$, enables changing of the relative amplitude of the spectral components of the voltage output, as we see later.

III. EXPERIMENTAL RESULTS

Equation (4) shows how large rf perturbations can be used to demonstrate a QD-based frequency multiplier. Due to the fixed resonance frequency of our resonator ($f_r \sim 789$ MHz), which acts as a sharp band-pass filter (see Appendix D), we fix the output frequency by setting the local oscillator (LO) used for homodyne mixing at f_r. To probe the various harmonics, we perturb the system via an rf signal along gate 2 at integer fractions of the frequency $f = f_r/N$ of the resonator. In Fig. 2, we show how the second and third harmonics evolve as a function of driving $\delta\epsilon$ and detuning offset ε_0 for a DTR transition and an ICT. We observe that all harmonics are symmetric along zero detuning (up to a phase of $(N+1)\pi$) and are characterized by N lobes in the magnitude response signal. For the even harmonics, the maximum voltage transfer

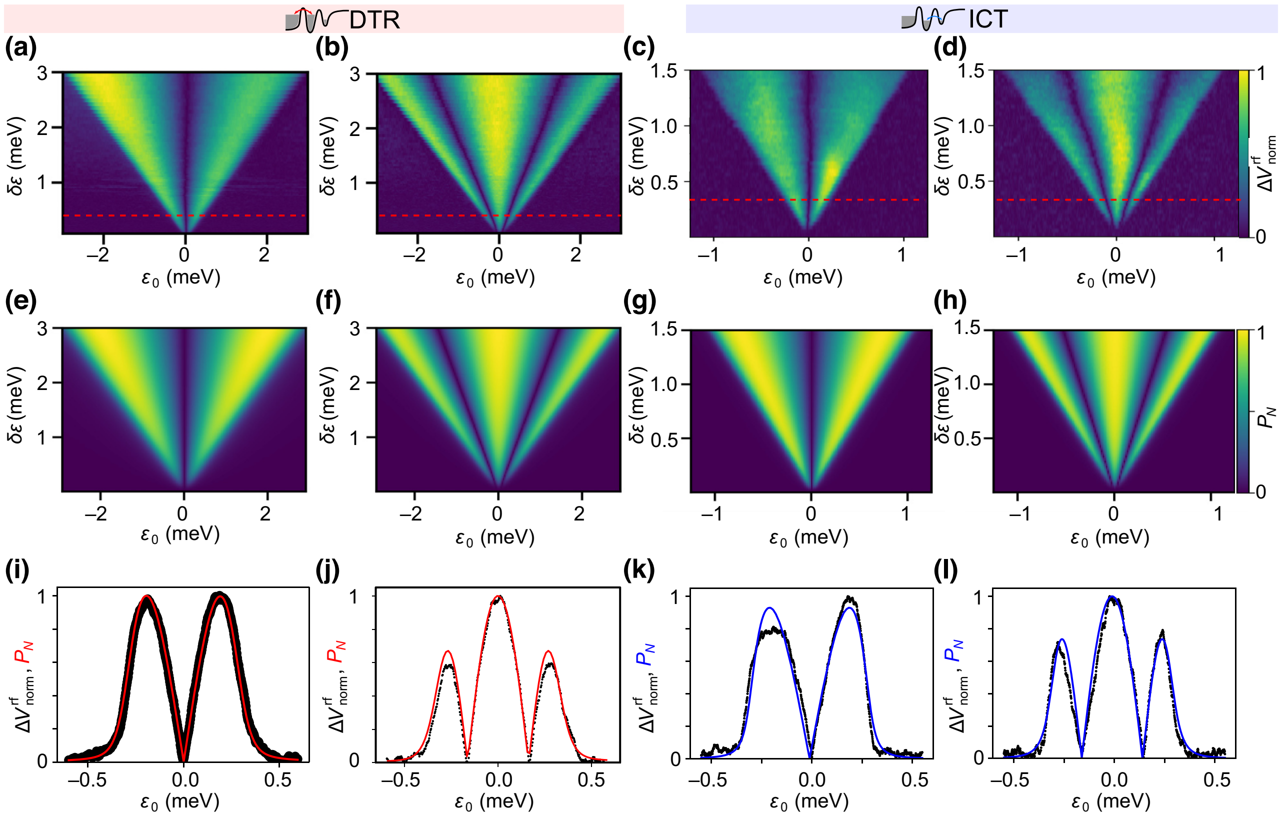

FIG. 2. QD-based frequency multiplier line shapes. (a)–(d) The experimentally measured (a),(c) second- and (b),(d) third- harmonic line shapes as a function of driving rf signal for the DTR transition and ICT, respectively. (e)–(h) Simulations of the corresponding panels above, carried out to demonstrate experimental agreement with the theory. (i)–(l) Line cuts at a driving rf amplitude of 0.37 meV peak to peak [red dotted line in (a)–(d)]. Data points are in black and the fits are solid lines.

occurs at $\varepsilon_0 = \pm\sin(\pi/N)\delta\varepsilon$ and is zero at $\varepsilon_0 = 0$ (see Appendix H). In contrast, for the odd harmonics, the signal is a maximum at $\varepsilon = 0$. As a result, the optimum detuning point to operate frequency multiplication varies for the different harmonics.

To accurately simulate the line-shape response for the various harmonics for both DTR transitions and ICTs, we develop a Lindblad framework. The method entails iterating the Lindblad master equation (LME) [33], defined as

$$\hbar\frac{d}{dt}\rho = -i[H(t),\rho] + \sum_{i=+,-}\hbar\Gamma_i\mathcal{D}[L_i], \tag{9}$$

with

$$\mathcal{D}[L_i] = L_i^\dagger\rho L_i - \frac{1}{2}\left\{L_i^\dagger L_i, \rho\right\} \tag{10}$$

to numerically obtain the QD-occupation probability $P(t) = \rho_{1,1}(t)$. Combined with Eq. (4), this allows us to simulate the rf-reflectometry line shapes without making use of the approximations in Eqs. (1) and (2). A mathematical derivation of the *jump* operators L_i and their relative relaxation rates Γ_i for the DTR transition and the ICT can be found in Appendix E. The gate lever arms ($\alpha_{\mathrm{dc}}\big|_{\mathrm{DTR}} = 0.56 \pm 0.05$ and $\alpha_{\mathrm{dc}}\big|_{\mathrm{ICT}} = 0.39 \pm 0.10$) and the electron temperature ($T_e = 160 \pm 5$ mK) are extracted experimentally in the small-signal regime (see Appendixes F–G), leaving the reservoir-dot relaxation rate Γ_R and the double-QD coupling term $\Delta = 2t_c$ as fitting parameters. At high frequencies, however, we must consider the capacitive coupling between the neighboring gates, which has no effect in dc. This, combined with the fact that $\alpha_{11} > \alpha_{21}$, gives rise to an *effective* rf lever arm of gate 2 on the QD along the DTR transition, with a value of $\alpha_{21}^{\mathrm{rf}} \approx 0.35$ (Appendix H). With these values, we use line shapes at constant rf power [Figs. 2(i)–2(l)] to fit $\Gamma_R = 2.9 \pm 0.6$ GHz and the ICT coupling term $\Delta = 35 \pm 9$ μeV.

Comparing Figs. 2(i)–2(l), we note the stark similarity of the line shapes of the DTR transition and ICT in the large-signal regime ($\delta\varepsilon = 0.37$ meV), which can be attributed to the same square-wave-like behavior of Eqs. (1) and (2). We see, however, slightly more pronounced sidebands in the ICT at the third harmonic when compared to the DTR transition. We attribute this to the lifetime broadening of the DTR transition (see Fig. 7 in Appendix F). By adding lifetime broadening to our model, we obtain excellent agreement with the experimental data [red line in Fig. 2(j)]. Moreover, comparing the data with the fits (blue lines) for the ICT, we observe an asymmetry with respect to $\varepsilon_0 = 0$, which is not present in the theory. We attribute this effect to not having swept the gate voltages perfectly along the detuning axis because of small errors in the calibration of the lever arms of gates 1 and 2 (and thus the direction of the sweep in voltage space) and the fact that the rf is applied only on gate 2 (see Appendix A).

We now move on to assess the performance of the QD-based frequency multiplier. First, we investigate the harmonic power-conversion efficiency using rf-voltage output maps equivalent to those shown in Fig. 2 up to $f_r/50$ (Appendixes P and Q). We quantify this efficiency by defining the figure of merit

$$\eta_{\max}(\delta\varepsilon) = \frac{\max_{\varepsilon_0}\left(|V_N^{\text{rf, out}}|^2\right)}{\max_{\varepsilon_0}\left(|V_1^{\text{rf, out}}|^2\right)}, \tag{11}$$

where $V_N^{\text{rf, out}}$ indicates the measured output voltage at the Nth harmonic. We choose this metric as it accounts for losses along the rf lines. We take the maximum signal for a given rf input power as the detuning ε_0 for optimal conversion, which depends on the specific harmonic of interest (Fig. 2). At $f_r/50$, a weak signal is still discernible for the DTR transitions but not for the ICTs, which we detect up to approximately $f_r/30$. We then extract the power-conversion efficiency for the different harmonics at a given input power (Appendix I). In Fig. 3(a), we plot the maximum power-conversion efficiency $\eta_{\max}$ compared to the first harmonic for the DTR transition and the ICT. The maximum power-conversion efficiency over all $\delta\varepsilon$ ($\max_{\delta\varepsilon}(\eta_{\max})$) follows the expected N^{-2} dependence for a square wave (black dotted line) until approximately $f_r/20$, above which $\max_{\delta\varepsilon}(\eta_{\max})$ begins to drop below the N^{-2} trend, as highlighted by the insert. We attribute the lower power-conversion efficiency observed at higher harmonics to the signal not being fully saturated at the maximum rf power used to probe the device. The ICT diverges from the N^{-2} dependence more drastically than the DTR transition due to a combination of factors. The first is our inability to drive the system as hard before excited states and multiple charge transitions start to interfere (see Appendix J). Second, there is a decrease in signal due to the less-pronounced nonlinearity for an ICT compared to a DTR transition (see Appendixes P and Q). The connection between the maximum power-conversion efficiency $\eta_{\max}$ and the maximum available output power can be found in Appendix K, where we discuss the effect of a load connected to the output of the QD multiplier device. In particular, we find that it behaves as an ideal current source as long as a large enough rf power can be applied to neglect the back action of the load on the collection gate. Most importantly, we discuss that with an optimized design and common device parameters, a $P^{N,\max} = -87 + 10\log_{10}(f\,[\text{GHz}]/N)$ dBm could be outputted, where $f = f_r/N$ is the excitation frequency (Appendix K).

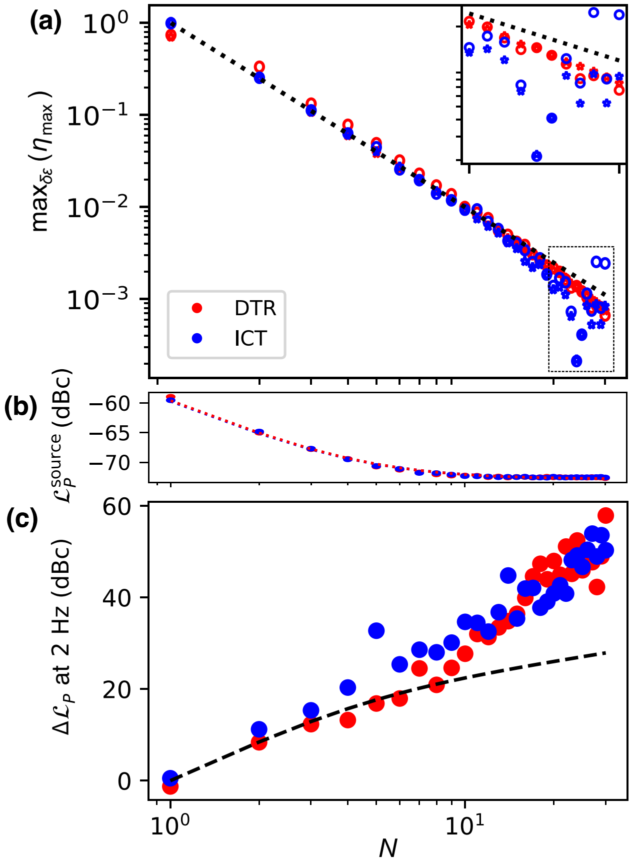

FIG. 3. The performance of a QD-based frequency multiplier. (a) The maximum power-conversion efficiency $\max_{\delta\varepsilon}(\eta_{\max})$ compared to the first harmonic for the DTR transition (red) and the ICT (blue) for increasing harmonic N. Experimentally measured values are plotted as circles and the fitted saturation points as stars. The first 20 harmonics closely follow an N^{-2} dependence (black dashed line). The inset is an enlargement of the region between $N = 20$ and $N = 30$. (b) The phase noise of the rf source at the relevant rf powers used for the DTR transition and ICT. The phase noise measured follows Leeson's equation (dotted line). (c) The difference in the phase noise between the rf source and the whole setup, which is attributed to the phase noise governed by the QD-based frequency multiplier, which increases as a function of the multiplication N. The black dotted line represents the ideal phase noise for a fully saturated signal (see Appendix L).

Another important metric for frequency multiplication is to assess the increase in phase noise $\mathcal{L}_p$ at higher harmonics. To calibrate our system, we measure the phase noise of the rf source, $\mathcal{L}_p^{\text{source}}$ [Fig. 3(b)], at the frequencies used to drive the DTR transition and ICT. The decrease in phase noise as we decrease the excitation frequency ($f = f_r/N$) follows the empirically established Leeson's equation [34] (red dotted line). In Fig. 3(c), the data show the phase-noise contribution of the QD-based frequency multiplier, $\Delta\mathcal{L}_p$, obtained by subtracting the rf source phase noise from the total phase noise measured. The harmonics produced by the driven QD system have an increasing phase noise as a function of the multiplication factor. Up to $N \sim 10$, the phase noise of our system is ideal (black dotted line), as defined in Appendix L; above this point, it diverges. The exact reason is unknown but we speculate that it is due to the output signal not being fully saturated. In this regime, additional phase noise may arise due to charge noise since the system is more sensitive to charge-probability variations as the occupation probability is not in a square-wave-like regime. The ideal frequency multiplication in the square-wave-like regime allows us to quantify the effect of quasi-dc fluctuators, such as charge noise or noise in the dc voltage. In particular, its only effect manifests in cycle-to-cycle jitter. In Appendix M, we show how a quantitative assessment of this effect leads to an estimate of the tolerable upper bound of the order of approximately 0.5 μeV over an integration bandwidth of an rf cycle, highlighting the excellent resilience of this device to dc noise. Moreover, in Appendix N we show how the impact of the stochastic nature of tunneling is an *additional* high-frequency noise term, which does not contribute to the phase noise. For slow electron tunneling compared to the excitation frequency, however, the effect becomes akin to shot noise. In this case, the signal and the intrinsic noise become comparable and performance of the multiplier may be degraded [35–38]. Additionally, we highlight how QD frequency multiplication, especially in the case of the ICT, can mostly be due to elastic charge transitions and thus operates almost without power dissipation.

Finally, we examine the performance of the multiplier when multiple charge transitions begin to merge above a given driving power ($P > 1$). In Fig. 4(a), we explore $N = 3$. We observe that at an excitation amplitude of approximately 4 meV, neighboring DTR lines begin to interfere, as two electrons are being loaded and unloaded in phase from the QD. Due to the N-1 nodes present in the phase of the Nth harmonic, constructive and destructive interference can occur, which can give rise to an increase in signal proportional to the number of tunneling electrons involved in the process, resulting in $\max_{\delta\varepsilon}(\eta_{\max})$ exceeding the expected N^{-2} dependence. Within this regime, the two-level system framework developed in Appendixes B and C is no longer valid. Therefore, the data in this regime are omitted from the $\max_{\delta\varepsilon}(\eta_{\max})$ and $\mathcal{L}_p$ discussion. We also observe the same interference behavior for the ICT, with the added phenomenon of having excited states appearing at certain driving rf powers, as outlined in Appendix J. Although harder to interpret, these regions of interference allow higher harmonics to be measured. We detect rf output signals up to $f_r/75$ (Appendix J).

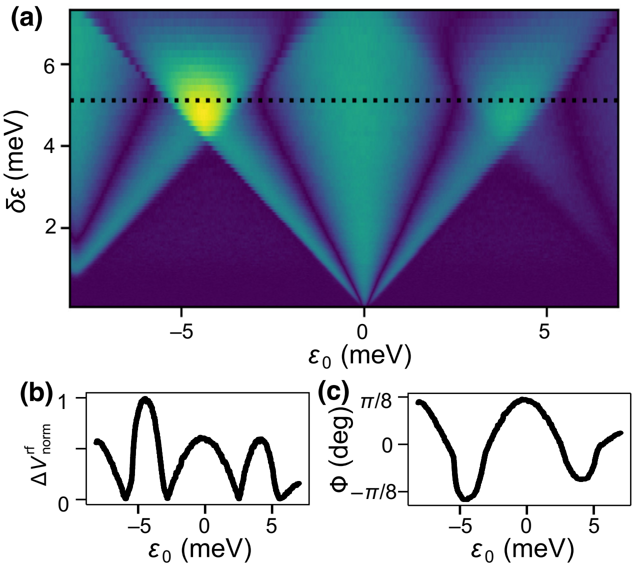

FIG. 4. Interference between multiple electron transitions. (a) The harmonic line shape for $f_r/3$ of multiple DTR lines as a function of the driving rf signal. (b),(c) By driving the system hard enough, the DTR lines interfere, resulting in regions of constructive interference with $\max_{\delta\varepsilon}(\eta_{\max})$ exceeding the expected N^{-2} dependence, as highlighted by the line cuts in (b) magnitude and (c) phase.

IV. CONCLUSIONS AND OUTLOOK

We introduce the idea of a QD-based frequency multiplier and demonstrate its experimental implementation via two methods: a QD coupled to a reservoir and a double QD. We find near-ideal performance in terms of power conversion and phase noise up to $N \approx 10$. The estimated output power of optimized QD-based frequency multipliers should allow the excitation of readout resonators (0.1–2 GHz) [39], the performance of circuit-QED experiments (4–8 GHz) [40], and approaches to the requirements for low-power electrically driven spin resonance (approximately 6 GHz) [41], although further developments may be needed for the latter, such as the use of constructive interference between different transitions presented here. By operating the multiplier in conjunction with a low-frequency generator, signal integrity may be better preserved from room temperature down to the mixing chamber of a dilution refrigerator and/or may facilitate the development of an integrated cryogenic frequency generator with dissipationless frequency multiplication. The latter is a prerogative of the quantum nature of the system and thus alleviates concerns on cooling power for future architectures. Furthermore, if combined with frequency mixing [42–44] and parametric amplification [24], one may envision an all-QD-based rf-reflectometry setup including frequency generation, amplification, and mixing.

With regard to the performance, we expect near-ideal properties as long as the electron tunneling process on which the operation of the multiplier is based remains elastic. This condition sets upper bounds for the maximum input frequency to $\omega \ll \Gamma_R$ in the DTR-transition case and $\Delta \gg \sqrt{\hbar\omega\delta\varepsilon}, k_BT$ for the ICT. The device remains operational at higher frequencies but additional dissipation may deteriorate its performance. However, we do not foresee these constraints limiting the usefulness of the device. In particular, there is no physical reason why Γ_R should be limited to a few gigahertz and $\Gamma_R = 70$ GHz has been experimentally observed [20], thus being able to operate in the microwave frequency range. One remaining challenge in this regime, however, is the band-pass filter. In this case, rather than a lumped-element resonator, distributed transmission-line-based design would be required [45–47]. Finally, we note that the large-signal regime explored here can be utilized for excited-state spectroscopy of (D)QD systems.

ACKNOWLEDGMENTS

This research was supported by the European Union Horizon 2020 research and innovation program under Grant Agreement No. 951852 [Quantum Large Scale Integration in Silicon (QLSI)] and by the United Kingdom Engineering and Physical Sciences Research Council (EPSRC) via the Cambridge EPSRC course for doctoral training in Nanoscience and Nanotechnology (NanoDTC) (EP/L015978/1), Quantum Engineering with Solid-State Technologies (QUES2T) (EP/N015118/1), Winton Programme for the Physics of Sustainability, the Hub in Quantum Computing and Simulation (EP/T001062/1) and Innovate UK [10000965]. M.F.G.Z. acknowledges a UK Research and Innovation (UKRI) Future Leaders Fellowship [MR/V023284/1].

APPENDIX A: CONSIDERATIONS ON LEVER ARMS

In the main text, we describe the general theory of QD-based frequency multiplication using three different lever arms: $\alpha_{\rm dc}$, $\alpha_{\rm rf}$, and α_c. We now detail how they relate to the quantities described in Appendixes G and H and their relationship to (D)QD detuning and gate current. Although common knowledge, in this work, these physical quantities are defined differently from the typical formulas used in the reflectometry literature, due to the use of different gates for excitation and collection. Thus, we explicitly derive the expression of lever arms for the DTR transition and ICT experiments. In the most general scenario, when a set of m gates is used to control n QDs, the detuning at which the quantized levels sit (for an arbitrary zero energy) can be written as

$$\vec{\varepsilon} = -e\underline{\underline{\alpha}}\vec{V}, \tag{A1}$$

where e is the elementary charge, $\underline{\underline{\alpha}}$ is the $n \times m$ lever-arm matrix, and $\vec{\varepsilon}$ and $\vec{V}$ are the energy and voltage vectors of length n and m, respectively. For ease of notation, we define $\vec{V} = \vec{0}$ when the relevant levels are all aligned (i.e., at zero detuning). Alternatively, Eq. (A1) can be understood as an affine linear transformation between voltage and energy space. In the case of the DTR transition, a single level is controlled in the following way: we control the dc detuning by sweeping gate 1, while gate 2 is used for rf delivery. Therefore, this corresponds to

$$\begin{aligned} \varepsilon_0\big|_{\rm DTR} &= e\alpha_{11}V_1 \\ \delta\varepsilon\big|_{\rm DTR} &= e\alpha_{\rm rf}\big|_{\rm DTR}\delta V_2(t). \end{aligned} \tag{A2}$$

The reason why we must consider $\alpha_{\rm rf}\big|_{\rm DTR} = \alpha_{21} + \gamma\alpha_{11}$ and not just α_{21} in ac is discussed in Appendix H. Finally, the gate current is collected via gate 1 and through the resonator acting as a band-pass filter. Therefore,

$$I_G\big|_{\rm DTR} = \alpha_{11}\frac{d}{dt}Q = e\alpha_{11}\frac{d}{dt}P. \tag{A3}$$

In the case of the ICT, two gates are used to sweep two QDs. Therefore,

$$\begin{pmatrix} \varepsilon_1 \\ \varepsilon_2 \end{pmatrix} = e\begin{pmatrix} \alpha_{11} & \alpha_{12} \\ \alpha_{21} & \alpha_{22} \end{pmatrix}\begin{pmatrix} V_1 \\ V_2 \end{pmatrix} \tag{A4}$$

As shown in the inset of Fig. 1, we sweep diagonally at −45° using both gate 1 and gate 2. This is achieved by maintaining

$$\begin{pmatrix} V_1 \\ V_2 \end{pmatrix} = \frac{V_0}{\sqrt{2}}\begin{pmatrix} 1 \\ -1 \end{pmatrix}$$

and therefore

$$\begin{pmatrix} \varepsilon_1 \\ \varepsilon_2 \end{pmatrix} = -\frac{1}{\sqrt{2}}eV_0\begin{pmatrix} \alpha' \\ -\alpha'' \end{pmatrix} \tag{A5}$$

where, similarly to Eq. (G3), we define

$$\begin{aligned} \alpha' &= \alpha_{11} - \alpha_{21}, \\ \alpha'' &= \alpha_{22} - \alpha_{12}. \end{aligned} \tag{A6}$$

Considering that the two gates are not perfectly identical, this gate configuration only *approximately* (although very closely; see Appendix G) sweeps orthogonally across the

ICT. The usual definition of ICT detuning in the literature is

$$\varepsilon_0\big|_{\mathrm{ICT}} = \vec{\varepsilon}\cdot\hat{n}, \tag{A7}$$

where $\hat{n}$ is the normalized vector orthogonal to the transition. By definition,

$$\hat{n} = \frac{1}{\sqrt{2}}\begin{pmatrix}1\\-1\end{pmatrix}$$

Thus, we conclude that the detuning along the ICT is defined by $\varepsilon_0\big|_{\mathrm{ICT}} = e\alpha_{\mathrm{dc}}\big|_{\mathrm{ICT}}V_0$, with

$$\alpha_{\mathrm{dc}}\big|_{\mathrm{ICT}} = \frac{\alpha' + \alpha''}{2}. \tag{A8}$$

Similarly to the DTR transition, also in the case of the ICT, the rf is delivered solely through gate 2. However, because of the capacitive coupling between the two gates (see Appendix H), we have

$$\begin{pmatrix}\delta\varepsilon_1\\ \delta\varepsilon_2\end{pmatrix} = -e\delta V_2(t)\begin{pmatrix}\gamma\alpha'\\ \alpha''\end{pmatrix}, \tag{A9}$$

with scalar detuning defined similarly as

$$\delta\varepsilon\big|_{\mathrm{ICT}} = \vec{\delta\varepsilon}\cdot\hat{n} \tag{A10}$$

or

$$\alpha_{\mathrm{rf}}\big|_{\mathrm{ICT}} = \frac{\alpha'' - \gamma\alpha'}{\sqrt{2}}. \tag{A11}$$

The effect of γ is to turn part of the rf excitation into a rigid shift of the DQD, which does not change the ICT detuning. Finally, as in the DTR transition, gate current is collected from gate 1. However, because this time charge flows into another dot, to which the gate is capacitively coupled, it is clear to see that

$$I_G\big|_{\mathrm{ICT}} = \alpha_{11}\frac{d}{dt}Q_1 + \alpha_{21}\frac{d}{dt}Q_2 = e\alpha'\frac{d}{dt}P_1. \tag{A12}$$

APPENDIX B: OCCUPATION IN THE LARGE-SIGNAL REGIME

The naive solution to the (D)QD occupation in the large-signal regime would be to assume a square-wave-like behavior, where the (D)QD is periodically emptied and filled if the rf amplitude is much larger than the detuning. This ansatz, however, fails due to the finite relaxation times of the respective systems. For the DTR transition, we can find an analytical expression for the large-signal regime through the master equation in Eq. (E9), the solution in the steady state is

$$P(t) = \Gamma_R e^{-\Gamma_R t}\int_{-\infty}^{t} e^{\Gamma_R \xi} f\left(\varepsilon(\xi)\right)d\xi, \tag{B1}$$

which can be expressed as the Fourier series

$$P(t) = f\left(\varepsilon_0\right) + \frac{1}{2}\sum_{n=1}^{\infty}\left(\frac{\Gamma_R}{\Gamma_R + iN\omega} f_N\, e^{iN\omega t} + \text{c.c.}\right), \tag{B2}$$

where

$$f_N = \frac{\omega}{2\pi}\int_0^{\frac{2\pi}{\omega}} e^{iN\omega t} f\left(\varepsilon_0 + \delta\varepsilon\cos\omega t\right)$$

is the Nth Fourier component of the perturbed Fermi-Dirac distribution. In the limit of fast relaxation ($\Gamma_R \gg \omega$), Eq. (B2) simplifies to $P(t) = f\left(\varepsilon(t)\right)$, which indeed tends to a square wave for large driving. For $\Gamma_R \sim \omega$, the coupling to the reservoir behaves as a low-pass filter for the square wave [see Fig. 5(a)]. In our particular experimental setup, we have a fixed resonator; thus $N\omega = \omega_r$ is constant. Therefore, the prefactor

$$\frac{\Gamma}{\Gamma + iN\omega} = \frac{\Gamma}{\Gamma + i\omega_r}$$

is just a global constant for all harmonics and all powers; thus all of the dynamics is described by f_N, which is square-wave-like.

For the ICT, we can consider a semiclassical solution in which the system evolves while remaining in the ground state. This represents the behavior of the ICT if the tunnel coupling is large enough to neglect Landau-Zener transitions (i.e., $\Delta^2 \gg \hbar\omega\delta\varepsilon$) [48] and relaxation events (i.e., $\Delta \gg \hbar\Gamma_P\left[2b(E)+1\right]$). In this case, we can simply write

$$P(t) = \frac{1}{2}\left[1 + \frac{\varepsilon(t)}{\sqrt{\varepsilon(t)^2 + \Delta^2}}\right] = \frac{1}{2}\left[1 + \Pi(t)\right], \tag{B3}$$

where $P(t)$ is the probability of the electron occupying the QD under the input gate. In the large-signal regime (i.e., $\delta\varepsilon \gtrapprox \Delta$), it is clear that $\Pi(t)$ tends to a square wave as the charge shifts from one QD to the other.

When considering the full model from the LME, we find the possible presence of Landau-Zener transitions when $\delta\varepsilon \approx \Delta^2/\hbar\omega$, which produce oscillations at the Rabi frequency $\Omega_R = (E_+ - E_-)/\hbar$. The result of these two effects produces a $P(t)$ that is formally no longer a square wave. However, we can gain insight into the effect of phonon relaxation in the system by considering the semiclassical

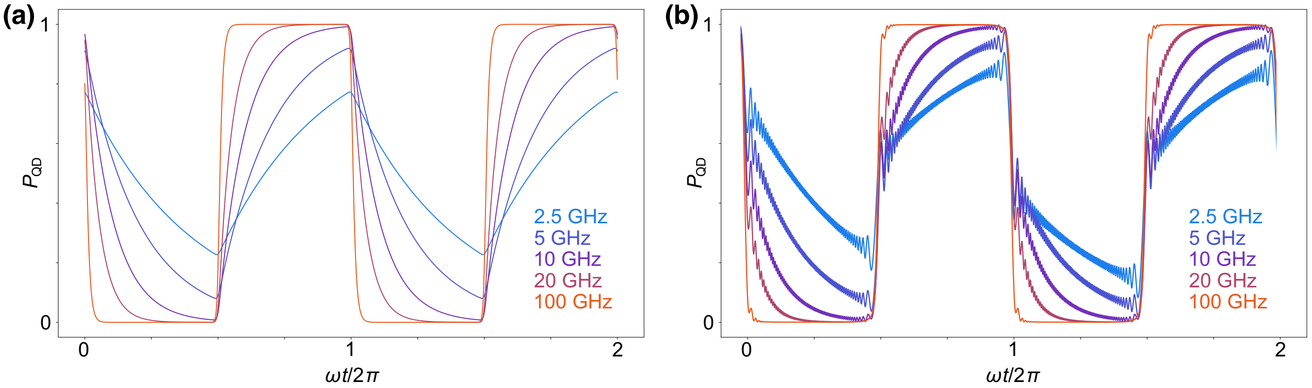

FIG. 5. Lindblad simulations (see Appendix E) of the steady-state QD occupation for (a) a DTR transition and (b) an ICT, for $\varepsilon_0 = 0$ and $\delta\varepsilon = 1$ meV at an rf frequency of $\frac{\omega}{2\pi} = 1$ GHz at 160 mK. The different curves indicate $\frac{\Gamma_R}{2\pi}$ for the DTR transition and $\frac{\Gamma_P}{2\pi}$ for the ICT. In (a), the electronic occupation of the QD evolves from a square wave for $\Gamma_r \gg \omega$ to a low-pass-filtered square wave for $\Gamma_R \sim \omega$, as predicted by Eq. (B2). In (b), in electronic occupation of one of the two QDs across an ICT (i.e., $\rho_{0,0}$(t)), the coupling term has been set to $\Delta = 35$ μeV as fitted from the experimental data. A comparison of (a) and (b) shows the qualitative similarity for the two systems as Γ approaches ω. However, additional high-frequency oscillations at the Rabi frequency $\frac{E_+ - E_-}{\hbar} \gg \omega$ appear as phonons that relax the system into the ground state after Landau-Zener transitions. We note that in these simulations, dephasing is intentionally ignored to emphasize this effect, which cannot be captured by semiclassical models.

approximation of the LME. In the basis where $H(t)$ is instantaneously diagonal (i.e., the *energy basis*), this reads

$$\dot{P}_{\mathrm{EB}} + \Gamma_P(2b(E(t)) + 1)P_{\mathrm{EB}} = \Gamma_P(b(E(t)) + 1), \tag{B4}$$

the formal solution of which is

$$P_{\mathrm{EB}}(t) = \Gamma_P e^{-\Gamma_{\mathrm{tot}}(t)} \int_{-\infty}^{t} e^{\Gamma_{\mathrm{tot}}(\xi)}(b(E(\xi)) + 1)d\xi, \tag{B5}$$

where we define

$$\Gamma_{\mathrm{tot}}(t) = \Gamma_P \int (2b(E(t)) + 1)dt. \tag{B6}$$

Projecting back into the QD basis, we can write

$$P(t) \approx \frac{1}{2}\Bigg[1 + \frac{1}{2n_0 + 1}\Pi(t) - \sum_{N=1}^{\infty}\left(\left(\left\{\frac{\Gamma_P(n_0+1)b_q}{\Gamma_P(2n_0+1) + iq\omega}\right\} * \{\Pi_q\}\right)_N e^{iN\omega t} + \text{c.c.}\right)\Bigg] \tag{B7}$$

where $(\{a_q\} * \{b_q\})_N$ indicates the Nth Fourier component of the convolution of the two Fourier series. Comparing the formal similarity of Eqs. (B1) and (B5), we can infer that the two systems will have comparable responses to an increasing relaxation rate. More thoroughly, it is possible to put a boundary on the effect of relaxation by considering that $|b_q| \leq b(2\Delta)/q$. In particular, in the large-signal regime $\delta\varepsilon \gg \Delta$, $b(E)$ is meaningfully different from zero only at the points in the cycle where $E(t) \lessapprox k_B T$. Therefore, the effect of the convolution is to add a finite slew rate to the square-wave-like response of $\Pi(t)$. Therefore, we ought to be able to neglect the effects of $b_{q>1}$, recovering the exact equivalence of the ICT with the DTR transition. This is highlighted in Fig. 5(b), which shows how the behavior of the ICT remains qualitatively similar to that of the DTR transition when including relaxation and for varying Γ_P. Moreover, we can see the fast oscillations at the Rabi frequency, which cannot be captured by the semiclassical nature of the master equation in Eq. (B4).

Following Eq. (B3), in the large-signal regime, we expect the main difference between the ICT and the DTR transition to be, apart from global constants, the substitution of $f(\varepsilon)$ with $\Pi(\varepsilon)$. The fact that the latter is a *polynomial* function of the energy explains the lower degree of nonlinearity observed for the ICT when compared with the exponential behavior of the Fermi-Dirac distribution in the DTR transition.

Moreover, for both systems, the square-wave behavior can be written as the Heaviside theta $\theta(\varepsilon(t))$. Therefore, if $\delta\varepsilon \geq |\varepsilon_0|$, it is trivial to predict the duty cycle as

$$\mathrm{DC} = \frac{1}{\pi}\arccos\left(\frac{\varepsilon_0}{\delta\varepsilon}\right). \tag{B8}$$

APPENDIX C: REFLECTOMETRY LINE SHAPES

The rf reflectometry measures charge transitions via changes in the reflection coefficient of a quantum system. In this work, we measure the *transmission* line shapes from gate 2 to gate 1, as detailed in Fig. 1. We can write the transmission coefficient as

$$T = \frac{2}{1 + YZ_0} \approx 2(1 - YZ_0), \tag{C1}$$

where $Z_0 = 50\ \Omega$ is the characteristic impedance of the line. Y is the effective admittance of the quantum system, where we can assume that $|Y|^{-1} \sim e^2/h \gg Z_0$. The quantum admittance can be modeled as the charge-dependent equivalent of the quantum capacitance and the Sisyphus resistance. For a particular harmonic N, the quantum admittance Y_N is defined as

$$Y_N = \frac{I_N}{\langle V \rangle} = 2\frac{\alpha_{\mathrm{rf}} e}{\delta\varepsilon} I_N, \tag{C2}$$

where $I_N = iN\omega P_N$ is the Nth Fourier component of the current through the device. Therefore, we can calculate the output of the rf measurement as

$$|\Delta V_N^{\text{rf, out}}| \approx |Y_N Z_0 V^{\text{rf, in}}| \propto \tag{C3}$$

$$\propto \left| \int_0^{\frac{2\pi}{N\omega}} e^{iN\omega t} P(t) dt \right|. \tag{C4}$$

Therefore, we can compute the rf line shapes of $P(t)$ either by numerically iterating the LME or from the expressions in Appendix B.

We must be aware that the above theory assumes a zero-dimensional discrete level with a deltalike density of states. In the case of the DTR transition, however, the coupling with the reservoir broadens the level. This can be modeled with an effective Lorentzian density $\mathcal{D}(E)$ of states with full width at half maximum (FWHM) Γ_R. This lifetime broadening becomes important when $\hbar\Gamma_R \gtrapprox k_B T$ and can be accounted for considering the convolution of $Y_N(\varepsilon_0)$ for the deltalike level with $\mathcal{D}(\varepsilon_0)$. The DTR transition of interest in this work is lifetime broadened, as discussed in Appendix F; therefore, this correction is used to fit the maps in Fig 14, with an estimated Γ_R of 2.9 ± 0.6 GHz.

APPENDIX D: FREQUENCY BAND-PASS FILTER

Due to the high-quality factor of the resonator, it acts as a narrow band-pass filter, meaning that even if the device is probed at multiple harmonics, we can only measure at the frequency of the resonator. To demonstrate this, we drive gate 2 at $f_r/2$ while sweeping the frequency of the local oscillator LO of the in-phase and quadrature (IQ) card around f_r, as shown in Fig. 6, illustrating the 5-MHz bandwidth of the resonator, within which we can obtain a signal. By plotting the in-phase (I) and quadrature (Q) components of the rf signal, we highlight how the line shape is antisymmetric, resulting in a phase component that can lead to constructive and destructive interference when multiple transitions overlap, as demonstrated in Fig. 4 and highlighted in Appendix J.

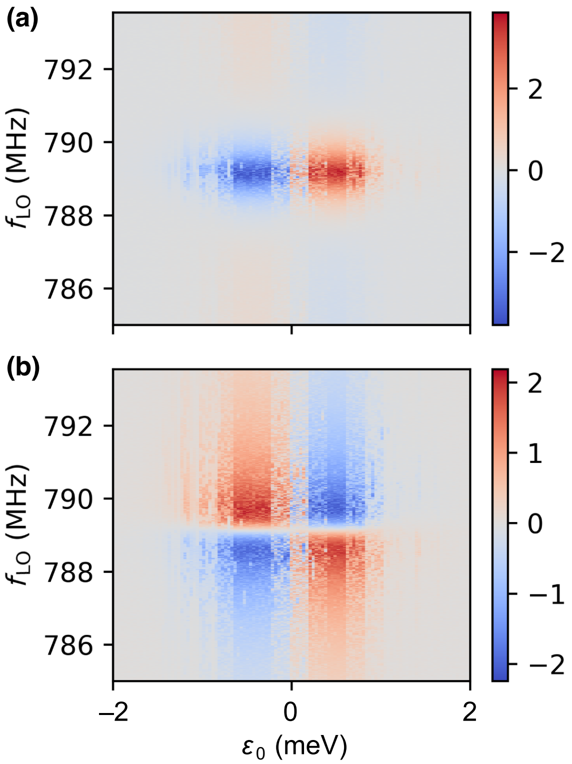

FIG. 6. The rf signal response in (a) I and (b) Q while probing $\omega_r/2$ at gate 2 and varying the LO frequency ω on a DTR transition.

APPENDIX E: LINDBLAD FORMALISM

To accurately simulate the behavior of the quantum systems in the nonlinear regime, we develop a model of the DTR transition and ICT based on the LME. In this context, the evolution of the density matrix is

$$\hbar\frac{d}{dt}\rho = -i[H(t), \rho] + \sum_{i=+,-} \hbar\Gamma_i \mathcal{D}[L_i], \tag{E1}$$

where

$$\mathcal{D}[L] = L_i^\dagger \rho L_i - \frac{1}{2}\left\{L_i^\dagger L_i, \rho\right\} \tag{E2}$$

describes the non-Hamiltonian part of the system evolution and its relaxation toward thermal equilibrium. These dynamics are fully described by a series of *jump operators* L_i and the relative coupling rates Γ_i. For the DTR transition, the Hamiltonian is

$$H(t) = \frac{1}{2}\begin{pmatrix} \varepsilon(t) & 0 \\ 0 & -\varepsilon(t) \end{pmatrix} \tag{E3}$$

and relaxation occurs via the electron reservoir, through an interaction Hamiltonian of the form

$$H_I = \hbar\Gamma_R(d^\dagger r + r^\dagger d), \tag{E4}$$

where d (r) is the fermionic destruction operator for an electron in the QD (reservoir). Equation (E4) gives rise to the jump operators

$$L_+ = d^\dagger = \begin{pmatrix} 0 & 1 \\ 0 & 0 \end{pmatrix}, \tag{E5}$$

$$L_- = d = \begin{pmatrix} 0 & 0 \\ 1 & 0 \end{pmatrix}, \tag{E6}$$

with the relevant rates being

$$\Gamma_+ = \Gamma_R f(\varepsilon), \tag{E7}$$

$$\Gamma_- = \Gamma_R (1 - f(\varepsilon)), \tag{E8}$$

where $f(\varepsilon)$ is the Fermi-Dirac distribution at the QD detuning. We note that, in the particular case of the DTR transition, the LME can be proven to be formally identical to the well-known semiclassical master equation [35]

$$\dot{P} + \Gamma_R P = \Gamma_R f(\varepsilon(t)), \tag{E9}$$

the analytical solution of which is discussed in Appendix C.

For the ICT, the presence of a tunnel coupling $\Delta = 2t_c$ in the DQD can be described by the Hamiltonian

$$H(t) = \frac{1}{2} \begin{pmatrix} \varepsilon(t) & \Delta \\ \Delta & -\varepsilon(t) \end{pmatrix}. \tag{E10}$$

In this case, the dominant relaxation process is phonon absorption and emission, which couple to the electronic system via

$$H_I = \hbar \Gamma_P (U d^\dagger U^\dagger a + a^\dagger U^\dagger d U), \tag{E11}$$

where a is the bosonic destruction operator of the phonon bath. In this model, we assume that phonon relaxation occurs between eigenstates of $H(t)$; hence we introduce the rotation matrix U, defined such that $U^\dagger H(t) U$ is always diagonal with eigenvalues

$$E_\pm(t) = \pm \frac{1}{2} \sqrt{\varepsilon(t)^2 + \Delta^2}, \tag{E12}$$

meaning that the energy difference between the ground and excited states is $E = E_+ - E_- = \sqrt{\varepsilon(t)^2 + \Delta^2}$.

Equation (E11) gives rise to the jump operators

$$L_+ = U d^\dagger U^\dagger \tag{E13}$$

$$L_- = U^\dagger d U \tag{E14}$$

with the relevant rates being:

$$\Gamma_+ = \Gamma_P b(E), \tag{E15}$$

$$\Gamma_- = \Gamma_P [b(E) + 1], \tag{E16}$$

where by $b(E) = \langle a^\dagger a \rangle = 1/(e^{E/k_B T} - 1)$ we indicate the Bose-Einstein distribution at the DQD energy splitting. It is also possible to include dephasing in this model with a rate Γ_ϕ through the additional jump operator

$$L_\phi = U \sigma_z U^\dagger. \tag{E17}$$

The effects of Γ_ϕ are to suppress coherent phenomena, such as Landau-Zener-Stueckleberg-Majorana interferometry, which are not discussed in this work. Numerically iterating Eq. (E1) allows for the simulation of $\rho(t)$, the Fourier transform of the diagonal entries of which, as a function of the detuning, is proportional to the rf-reflectometry line shapes.

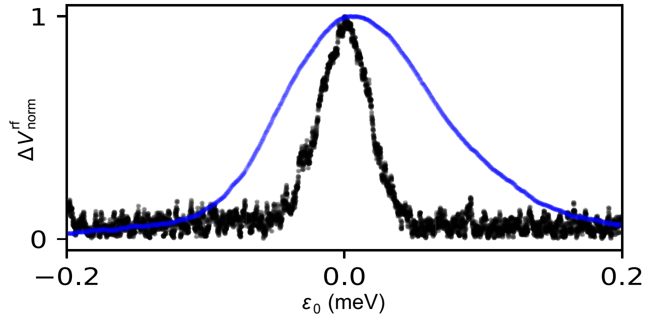

FIG. 7. The experimentally measured DTR line shapes in the thermally (black) and lifetime (blue) broadened regimes, normalized to their maximum value.

APPENDIX F: ELECTRON TEMPERATURE

To set an upper bound for the electron temperature T_e, we find the narrowest DTR transition (black line in Fig. 7) on the QD under V_{g1} and measure its FWHM as a function of the mixing-chamber fridge temperature T_{fridge}. We tune the device to a different region in voltage space, where the signal is narrower than the lifetime-broadened DTR transition used for multiplication (see Fig. 7).

We ensure no power broadening by measuring the transition at varying rf powers [22]. From the temperature-dependence measurements in Fig. 8, we fit the following expression to extract T_e (red curve in Fig. 8):

$$\text{FWHM} = \frac{3.53 k_B}{e\alpha_{11}} \sqrt{T_{\text{fridge}}^2 + T_e^2}. \tag{F1}$$

From the fit, we extract the electron temperature of $T_e = 160 \pm 5$ mK and the lever arm $\alpha_{11} = 0.56 \pm 0.05$.

APPENDIX G: dc LEVER-ARM EXTRACTION

To extract the other lever arms, we can use the stability map; in conjunction with our knowledge of α_{11}. In particular, we know from the constant-interaction model that the slopes of the transitions read

$$\left.\frac{dV_{g2}}{dV_{g1}}\right|_{\mathrm{ICT}} = \frac{\alpha_{11}-\alpha_{21}}{\alpha_{22}-\alpha_{12}} = \frac{\alpha'}{\alpha''} = 0.99 \pm 0.05, \tag{G1}$$

$$\left.\frac{dV_{g2}}{dV_{g1}}\right|_{\mathrm{DTR}_{g1}} = -\frac{\alpha_{11}}{\alpha_{12}} = -3.3 \pm 0.6, \tag{G2}$$

$$\left.\frac{dV_{g2}}{dV_{g1}}\right|_{\mathrm{DTR}_{g2}} = -\frac{\alpha_{21}}{\alpha_{22}} - 0.32 \pm 0.03, \tag{G3}$$

where the numerical values are obtained from Fig. 9(a). We can then reconstruct the whole lever-arm matrix, as

$$\begin{pmatrix} \alpha_{11} & \alpha_{12} \\ \alpha_{21} & \alpha_{22} \end{pmatrix} = \begin{pmatrix} 0.56 \pm 0.05 & 0.16 \pm 0.04 \\ 0.17 \pm 0.05 & 0.55 \pm 0.06 \end{pmatrix}. \tag{G4}$$

We also independently consider the ICT and the DTR on gate 1 used for the frequency-multiplication experiments. The agreement between the measured values and the stability maps in those regions is shown in Figs. 9(b) and 9(c).

APPENDIX H: ac LEVER-ARM EXTRACTION

From fitting the detuning ε_0 versus driving $\delta\varepsilon$ maps, such as those in Fig. 2, we can experimentally determine the high-frequency lever arms as well as estimate the power loss of the fast lines. These can differ from those measured in dc because of different cross-capacitive couplings at high frequencies between the gates. Moreover, in the case $N = 1$, the rf voltage arising on gate 1 due to the capacitive coupling with gate 2 can be amplified by the resonator. This effect can be measured by comparing the slope $\varepsilon_0(\delta\varepsilon)$ where the power conversion of the Nth harmonic is zero. From Eq. (8), the $N-1$ zeros of the Nth harmonic should occur for

$$\varepsilon_0 = \cos\left(\pi\frac{m}{N}\right)\delta\varepsilon \quad m = 1, \ldots, N-1. \tag{H1}$$

We also note that the N maxima are predicted to appear for

$$\varepsilon_0 = \cos\left(\pi\left(\frac{m}{N}+\frac{1}{2}\right)\right)\delta\varepsilon \quad m = 0, \ldots, N-1. \tag{H2}$$

The effect of cross-capacitance is more easily considered in the case of the DTR transition, where coupling between the gates leads us to define an *effective* rf lever arm

$$\left.\alpha_{\mathrm{rf}}\right|_{\mathrm{DTR}} = \alpha_{21}^{\mathrm{dc}} + \gamma\alpha_{11}^{\mathrm{dc}}, \tag{H3}$$

where γ is a coupling term between 0 and 1 for $N > 1$ and between 0 and the quality factor of the resonator Q for the first harmonic (Fig. 11). All harmonics except the first show $\gamma \sim 0.5$, which corresponds to $\left.\alpha_{\mathrm{rf}}\right|_{\mathrm{DTR}} \approx 0.35$. We attribute the large discrepancy of the first harmonic to direct cross-coupling to the resonator from the input gate 2 to gate 1, which results in a larger effective lever arm.

Finally, the expression for $\left.\alpha_{\mathrm{rf}}\right|_{\mathrm{ICT}}$ derived in Eq. (A11) allows us to fit the data sets in Figs. 2(g) and 2(h) for the attenuation down the fridge in addition to the nominal values present on the line (see Fig. 10), which we estimate as 0.7 ± 0.1 dB.

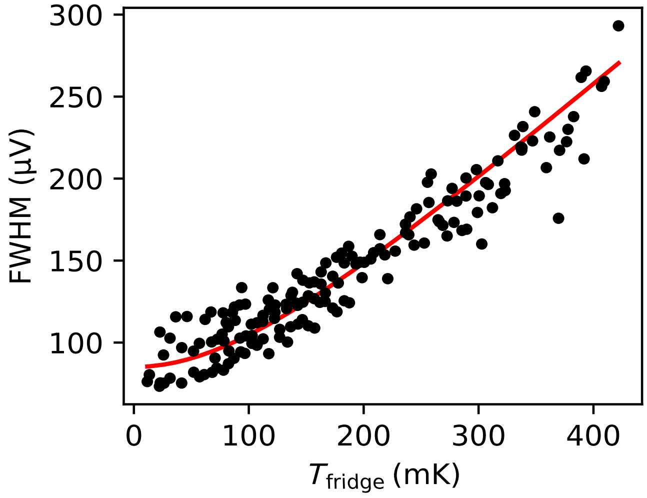

FIG. 8. The temperature dependence on the FWHM of a DTR transition on gate 1, from which an electron temperature T_e of 160 ± 3 mK is extracted.

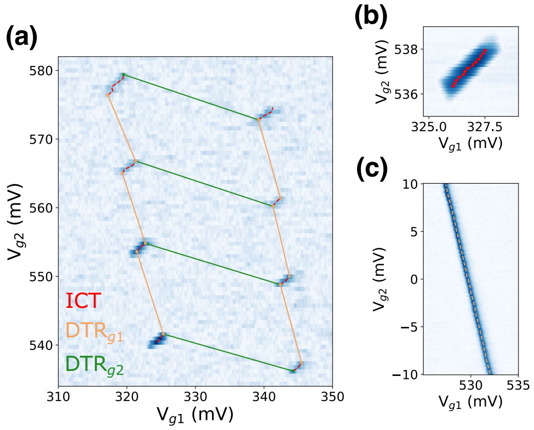

FIG. 9. The slopes from the stability maps are used to extract the lever-arm matrix from α_{11}. (a) The region of the stability maps from which the slopes are extracted. (b),(c) The (b) ICT and (c) DTR_{g1} that are used to perform the frequency-multiplication measurement. The superimposed lines are traced with the values extracted from (a) to check for consistency.

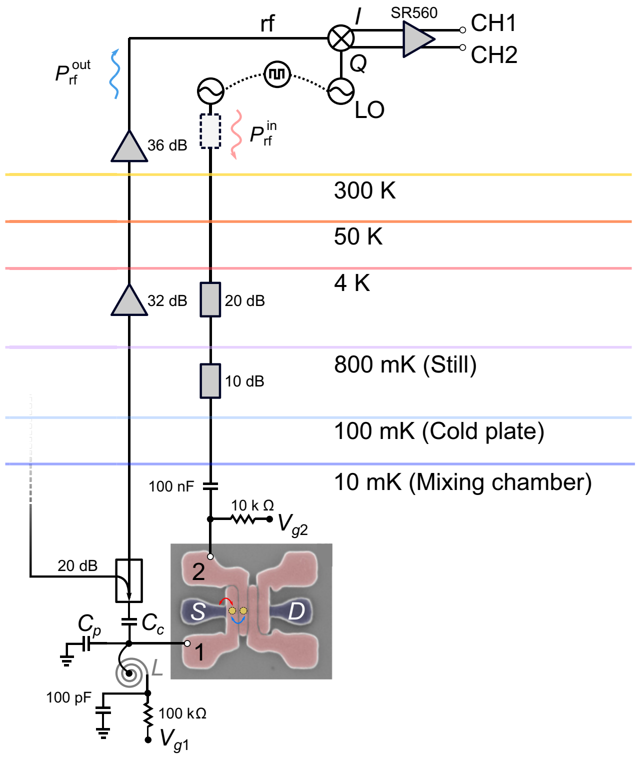

FIG. 10. A schematic of the dilution-unit setup with all relevant attenuators and amplifiers. The line on gate 2 (furthest to the right) is used for frequency multiplexing. The dashed squared rectangle at the rf input line ($P_{\rm rf}^{\rm in}$) is a 30-dB attenuator for the first harmonic and a low-pass filter of 450, 300, 200, 100, or 70 MHz depending on the harmonic being measured. The clocks of both rf sources are synchronized to ensure that they are in phase.

APPENDIX I: POWER-CONVERSION-EFFICIENCY EXTRACTION

The measurements in Appendixes P and Q are used to extract the power-conversion efficiency for the DTR transition and ICT. The acquired data are limited to rf powers where no excited states or interference between multiple transitions are present (see Appendix J). The maximum signal will then occur at zero detuning for the odd harmonics, while for the even ones, it depends linearly on $\delta\epsilon$. For each harmonic, we extract the measured maximum signal at each rf power along with the corresponding fitted value, as shown in Fig. 12. These are then used to plot the power-conversion relationship shown in Fig. 3(a).

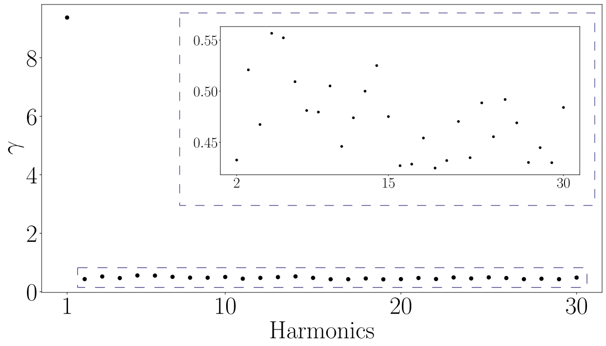

FIG. 11. The coupling term γ, defined using Eq. (H3), obtained from fitting the $\delta\varepsilon$ versus ε_0 maps. As expected, γ is an order of magnitude larger for the first harmonic because of the presence of the resonator, while $\gamma \sim 0.5$ for N>1 (shown in the inset). This value corresponds to an ac lever arm of $\alpha_{\rm DTR}^{\rm rf} \approx 0.35$.

APPENDIX J: N^{-2} DEPENDENCE

At high powers, it is possible to drive the system strongly to overcome the expected power-conversion dependence of N^{-2}. In particular, for the ICT, an increment in signal is possible if excited states are present, as shown in Fig. 13(a). This is due to a gain in quantum capacitance due to an increase in curvature of the eigenenergies. By driving the system even harder, it is possible to obtain multiple charges n to transition, resulting in an interference pattern, as highlighted in Fig. 13(b). We can thus find regions in voltage that should theoretically result in an increase of n in power conversion that will counteract the expected N^{-2} relationship; this allows us to measure a signal at even higher harmonics, such as $f_r/75$, as shown in Fig. 13(c).

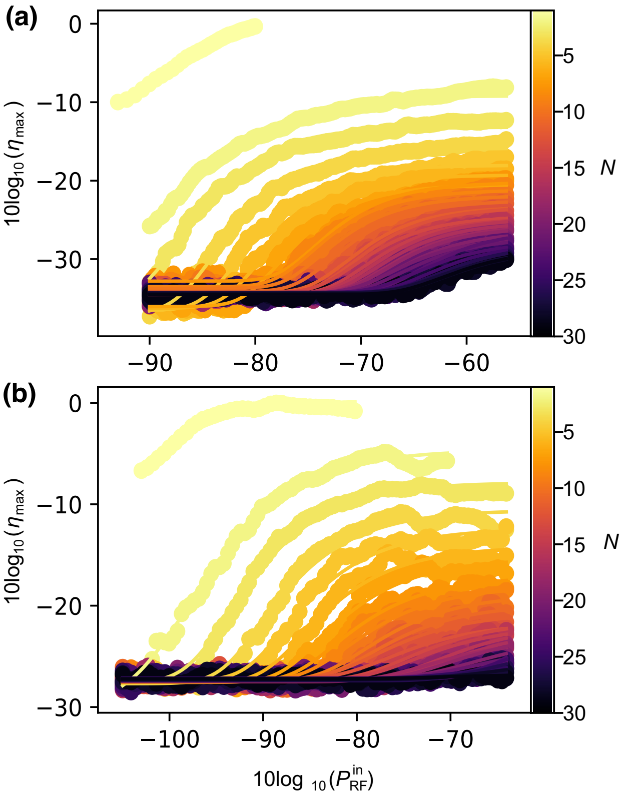

FIG. 12. The power conversion measured for the first 30 harmonics for (a) the DTR transition and (b) the ICT that are used to extract the data in Fig. 3(a).

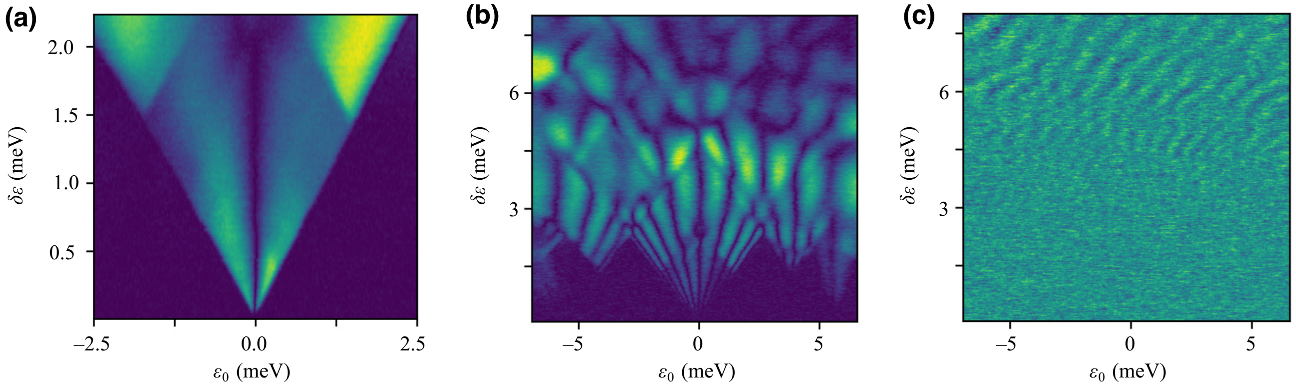

FIG. 13. Increasing the power conversion above the expected N^{-2} dependence. (a) The second-harmonic ICT transition, highlighting how an increase in power conversion is obtainable due to the presence of excited states above a driving detuning $\delta\epsilon \sim 1.5$ meV. (b) the tenth harmonic, showcasing how multiple ICTs can interfere at high enough detunings. By modulating multiple electrons, an increase in power conversion is possible, resulting in regions of constructive interference. (c) The measured signal at $\omega_r/75$ obtained from the interference of multiple ICT transitions.

APPENDIX K: MAXIMUM OUTPUT POWER

Considering the potential technological applications of the proof of concept presented in this work, we see fit to evaluate the maximum achievable output power for a QD multiplier. Since for the Fourier terms of a square wave $A_N \leq 1/N\pi$, by using Eq. (3), we can write the maximum achievable gate current for the Nth harmonic as

$$I_g^{N,\max} = \frac{e\alpha_c}{N\pi}\omega_r = \frac{2e\alpha_c}{N}f_r. \tag{K1}$$

In the current setup, where this resonator is used for reflectometry readout, we require matching the impedance of the readout circuit at resonance to that of the line. In particular, the readout network is engineered so that the gate sees an impedance to ground $Z_{\mathrm{BP}} \approx Z_0 = 50\Omega$, with the equality holding for a perfectly matched resonator [20]. This impedance matching is not required to operate a QD device for frequency multiplication and the filtering assembly can be optimized for both performance and footprint. If we assume that the QD multiplier is used to drive a load with impedance Z_L to ground (including the band-pass filter), it is trivial to write the maximum voltage as

$$V^{N,\max} = \frac{2e\alpha_c}{N}f_r Z_L, \tag{K2}$$

from which the maximum transferred power is

$$P^{N,\max} = \left(I_g^{N,\max}\right)^2 Z_L = \left(\frac{2e\alpha_c}{N}f_r\right)^2 Z_L. \tag{K3}$$

From Eq. (11), it ought to be clear that the measured output power can be read directly from Fig. 3 as

$$P^N = \max_{\delta\varepsilon}(\eta_{\max})\ (2e\alpha_c f_r)^2\ Z_L. \tag{K4}$$

The fact that the output power can be made arbitrarily large is a direct consequence of the assumption that the *collection* branch of the circuit is operating in the small-signal regime. In general, the detuning seen by the QD system is

$$\varepsilon(t) = \varepsilon_0 + \delta\varepsilon\cos\omega t + \varepsilon_{BA}(t),$$

where

$$\varepsilon_{BA}(t) = e\alpha_c V_{\mathrm{out}}(t),$$

which is the back action of the load on the system. The treatment in this work is valid as long as this is a negligible perturbation of the rf. More quantitatively, we require

$$\varepsilon_{BA}(t) \ll \delta\varepsilon$$

or

$$Z_L \ll \frac{\alpha_{\mathrm{rf}}}{\alpha_c^2}\frac{V^{\mathrm{rf,in}}}{2ef_r}, \tag{K5}$$

where $V^{\mathrm{rf,in}}$ is the amplitude of the applied rf driving. Perhaps counterintuitively, comparing Eqs. (K2) and (K5), we see how increasing the rf power has no benefit in increasing the gate current but, rather, on the maximum load that the system can drive. This is an inherent property of the discrete nature of the quantum levels, the occupation of which is fixed by Coulomb blockade and the quantization of charge. However, as long as the energy swing is large enough to guarantee a transition twice per rf cycle, the system will act as a current generator. We note that the upper bound for $V^{\mathrm{rf,in}}$ is determined by the Coulomb-blockade effect; if the amplitude is large enough to be comparable to the QD charging energy, multiple electron transitions can

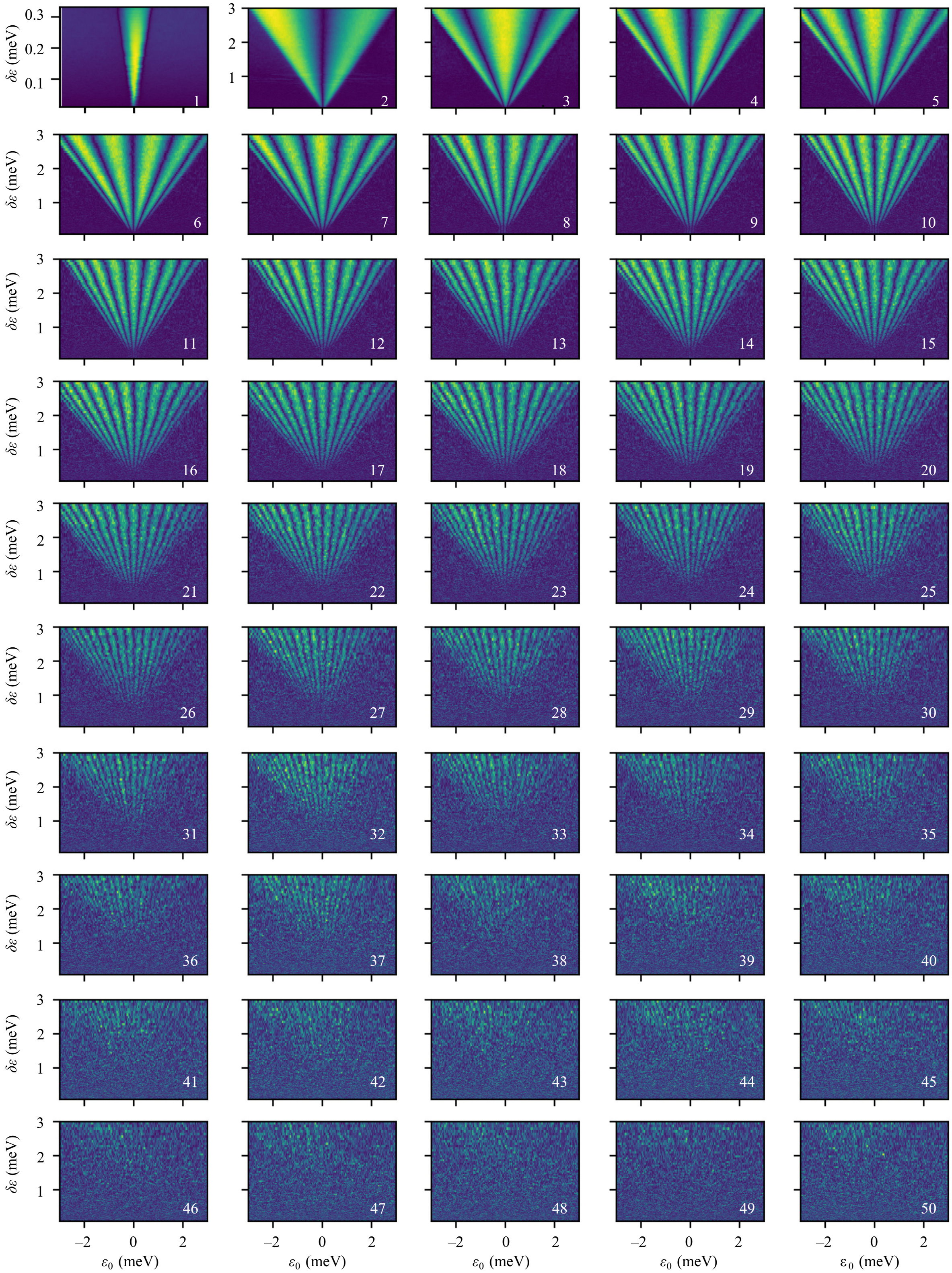

FIG. 14. The raw data of the first 50 harmonics experimentally measured across a DTR transition.

TABLE I. A measure of harmonic rejection (dBc) in the case of the DTR transition for an input power of −60 dBm.

	Measurement frequency, ω_r/N_M									
Driving frequency, ω_r/N_D	1	2	3	4	5	6	7	8	9	10
1	0									
2	0	−68								
3	0		−79							
4	0	−68		−126						
5	0				−133					
6	0	−67	−79			−129				
7	0						−132			
8	0	−60		−126				−136		
9	0		−68						−135	
10	0	−60			−138					−138

occur. As a rough estimate, this will happen when the load impedance has a value

$$Z_L \approx \frac{\alpha_{\mathrm{rf}}}{\alpha_c^2}\frac{1}{2f_rC_g}, \tag{K6}$$

i.e., when Z_L is comparable to the impedance of the driving gate (with gate capacitance C_g). Considering the discussion in Appendix J, however, the insurgence of other transitions is not an issue but, rather, is exploited to create positive interference between two (or more) electrons to increase the maximum gate current beyond Eq. (K1).

Finally, we estimate typical values $P^{N,\max}$. By substituting Z_L into Eq. (K3), we obtain the maximum output power

$$P^{N,\max} = \left(\frac{2e\alpha_c}{N}f_r\right)^2 Z_L \approx \frac{2e^2\alpha_{\mathrm{rf}}f_0}{C_gN}, \tag{K7}$$

where we remind the reader that $f_r = Nf_0$ is the output frequency, while, for clarity, we indicate the driving frequency by f_0. By using $\alpha_{\mathrm{rf}} = 0.35$ (as extracted in the main text), $C_g = 10$ aF (a typical value reported in the literature [49]), we obtain

$$P^{N,\max} = -87 + 10\log_{10}\left(\frac{f_0[\mathrm{GHz}]}{N}\right)\ \mathrm{dBm} \tag{K8}$$

or

$$P^{N,\max} = -87 + 10\log_{10}\left(\frac{f_r[\mathrm{GHz}]}{N^2}\right)\ \mathrm{dBm}, \tag{K9}$$

where both are given if, given design constraints, one prefers to consider the input or the output frequency. If we assume a driving of $f_0 = 1$ GHz, for example, we obtain $P^{N,\max} = -87 - 10\log_{10}(N)$ dBm $\approx$ 2 pW/N.

We can now consider the power output in realistic applications. In the case of magnetically driven electron-spin-resonance experiments, −40 to −20 dBm of on-chip power is required between 1 and 50 GHz [15]. If we take $f_r \approx 40$ GHz, then $P^{N,\max} = -72 - 20\log_{10}(N)$ dBm. Therefore, approximately 40 dB of amplification would be required, thus making the frequency multiplier an unpractical solution. However, electric dipole spin resonance (EDSR) measurements may be within reach. For $f_r \approx 6$ GHz, $P^{N,\max} = -78 - 20\log_{10}(N)$ dBm. Microwave powers as low as −90 dBm at 5.8 GHz have been reported [41], for which a QD-based frequency multiplier could be utilized, although it may be pushing the limit of what is practically feasible.

In the case of reflectometry, we can assume $f_r \approx 2$ GHz and thus $P^{N,\max} = -85 - 20\log_{10}(N)$ dBm; therefore a QD-based frequency multiplier should be more than adequate, with optimum powers for spin readout reported to be as low as −110 dBm [20] and certainly suitable for circuit-QED experiments in the few-photon limit, at −140 dBm [40].

APPENDIX L: IDEAL PHASE NOISE

The phase noise of an rf source dominated by $1/f$ noise can be empirically described by Leeson's equation [34],

$$\mathcal{L}_p(\omega_0, \Delta\omega) = 10\log\left[\frac{2Fk_BT}{P_{\mathrm{sig}}}\left(1 + \frac{\omega_0}{2Q\Delta\omega}\right)^2 \times\left(1 + \frac{\Delta\omega_{1/f^3}}{|\Delta\omega|}\right)\right], \tag{L1}$$

where $\Delta\omega$ is the offset frequency from the carrier frequency ω_0, F is an empirically fitted parameter known as the noise factor, P_{sig} is the power of the rf source, Q is the loaded quality factor, and $\Delta\omega_{1/f^3}$ is the $1/f$ corner frequency. The $\omega_r/2Q\Delta\omega$ dependence arises from the $1/f$ decrease in the voltage-frequency response for an ideal *RLC* tank circuit as a function of $\Delta\omega$, which is then squared to convert it into power. The noise factor F and the additive 1 within the first set of brackets account for the noise floor. The second parentheses provide the $1/|\Delta\omega|^3$ behavior observed at limited offset frequencies.

An ideal frequency multiplier performs a rigid shift in the frequency axis, which, after multiplication, increases the phase noise by a factor of N. For harmonics at the same frequency offset $\Delta\omega$, as is the case in our data in Fig. 3, the ideal phase noise is

$$\Delta\mathcal{L}_p^{N,\text{ideal}} = \mathcal{L}_p\left(\frac{\omega_r}{N}, \frac{\Delta\omega}{N}\right) - \mathcal{L}_p\left(\frac{\omega_r}{N}, \Delta\omega\right). \tag{L2}$$

APPENDIX M: IMPACT OF dc NOISE IN PHASE NOISE

As mentioned in Sec. III, it is easy to see that, at saturation, the only impact of dc noise would be on the definition of ε_0 and, therefore, the point of the cycle at which the charge transition occurs. In a square-wave signal, this manifests as jitter noise. If we assume dc noise to be Gaussian distributed with variance σ_ε, its effect on $\Delta\mathcal{L}_p$ around the Nth harmonic would be almost Lorentzian, with

$$\text{FWHM} = \pi N f_r \sigma_{\text{dc}}^2 \approx \pi N f_r \left(\frac{\sigma_\varepsilon}{\delta\varepsilon}\right)^2,$$

where σ_{dc}^2 is the cycle-to-cycle jitter [50]. The relation between σ_ε and σ_{dc} can be obtained from Eq. (8). From our measurements of phase noise, we observe a FWHM of approximately 5 Hz. Considering the use of $\delta\varepsilon \sim 1$ meV, this gives us an upper bound of the dc noise in the detuning of about $\sigma_\varepsilon \sim 0.5$ μeV. We stress that this figure derives from the cycle-to-cycle jitter and thus must be understood as integrated over a measurement time of one rf cycle. Typical figures of charge noise in silicon QDs are $1 - 10$ μeV, with an integration bandwidth of 1 Hz [51]. Thus, the system is highly resilient to (quasi-)dc noise, which is consistent with experimental observation. The noise limit can be qualitatively understood by the fact that noise in the detuning ε_0 (given by either noise in the dc voltage or charge noise) can be considered as an *effective temperature* and that, in the large-signal regime, the saturation behavior is well described by Eq. (7), where the temperature is not present. Physically, this is supported by the intuition that if $\delta\varepsilon$ is larger than any thermally induced broadening, we can treat the Fermi function as a step function for the DTR transition and ignore photon absorption for the ICT.

APPENDIX N: CONSIDERATIONS ON THE STOCHASTIC NATURE OF TUNNELING

In this appendix, we briefly address the matter of the stochastic nature of electron tunneling and how that gets reflected in the performance of a QD as a frequency multiplier. In the following, we focus on the DTR transition for its ease of calculation due to the master equation in Eq. (E9). First and foremost, since Eq. (E9) is a master equation, the (average) gate current calculated as in Eq. (3) remains valid and only depends on the assumptions that, on the time scales of the rf, the response of the QD is Markovian and the reservoir is always in thermal equilibrium. Therefore, the stochastic nature of tunneling will introduce an additional *intrinsic* noise, which is generated by the device. This can be easily obtained in the large-signal regime, i.e., $\delta\varepsilon \gg \Gamma_R, k_BT$, if we note that Eq. (E9) is formally the same as a single electron source. Therefore, we can use a known result to obtain the (two-sided) current noise power spectral density (PSD) as [35–38]

$$S_I(\omega) = \frac{\omega_0}{\pi}\tanh\left(\frac{\pi\Gamma_R}{2\omega_0}\right)\frac{(\alpha_c e\omega)^2}{\Gamma_R^2 + \omega^2}, \tag{N1}$$

where ω_0 is the driving frequency. Experimentally, we are only interested in the noise PSD around the frequency of the band-pass filter $\omega \approx \omega_r = N\omega_0$, as everything outside its bandwidth will be filtered out. Notably, Eq. (N1) is an *additional* noise term, which does not contribute directly to the phase noise since it does not peak at any of the harmonics. The stochastic nature of this term becomes evident if we consider its limiting behavior for both small and large tunneling rates.

If $\Gamma_R \gg \omega_0$, then $\tanh(\pi\Gamma_R/2\omega_0) \approx 1$. In this case, one electron can always tunnel every half cycle and the noise term is given by the phase jitter of the tunneling event occurring at random points in a cycle. In this case, the noise is intrinsically high frequency, a typical phenomenon of single-charge emission [36]. Interestingly, for a small filter bandwidth $\Delta\omega_r$, the ratio of the signal to the intrinsic noise (SNR_I) of the output power of the multiplier reads

$$\text{SNR}_I \approx \frac{|I_N|^2}{S_I(\omega_r)\Delta\omega_r} \approx \frac{Q_r}{\pi N^3}\left(\frac{\Gamma_R}{\omega_0}\right)^2, \tag{N2}$$

where $Q_r = \omega_r/\Delta\omega_r$ is the band-pass quality factor and I_N is the Nth Fourier component of the signal current. For the benefit of the reader, we recall from Appendix K that, in the large-signal regime, one can approximate

$$|I_N| \approx \frac{\alpha_c e}{N\pi}\frac{\omega_r\Gamma_R}{\sqrt{\omega_r^2 + \Gamma_R^2}}, \tag{N3}$$

from which we also see how the regime $\Gamma_R \gg \omega_r$ is the most favorable in terms of the output power.

In the opposite limit, $\Gamma_R \ll \omega_0$ (and thus $\Gamma_R \ll \omega_r$), the hyperbolic tangent dominates, as electrons *fail to tunnel* every cycle. Notably, in the case of very slow electron tunneling, S_I becomes constant in frequency and

$$S_I = \frac{(\alpha_c e)^2}{2}\Gamma_R = (\alpha_c e)^2 f_0 P_{\text{tun}}, \tag{N4}$$

where $P_{\text{tun}} = \Gamma_R/2f_0$ electron tunneling probability per half cycle and $f_0 = \omega_0/2\pi$ is the frequency of the drive.

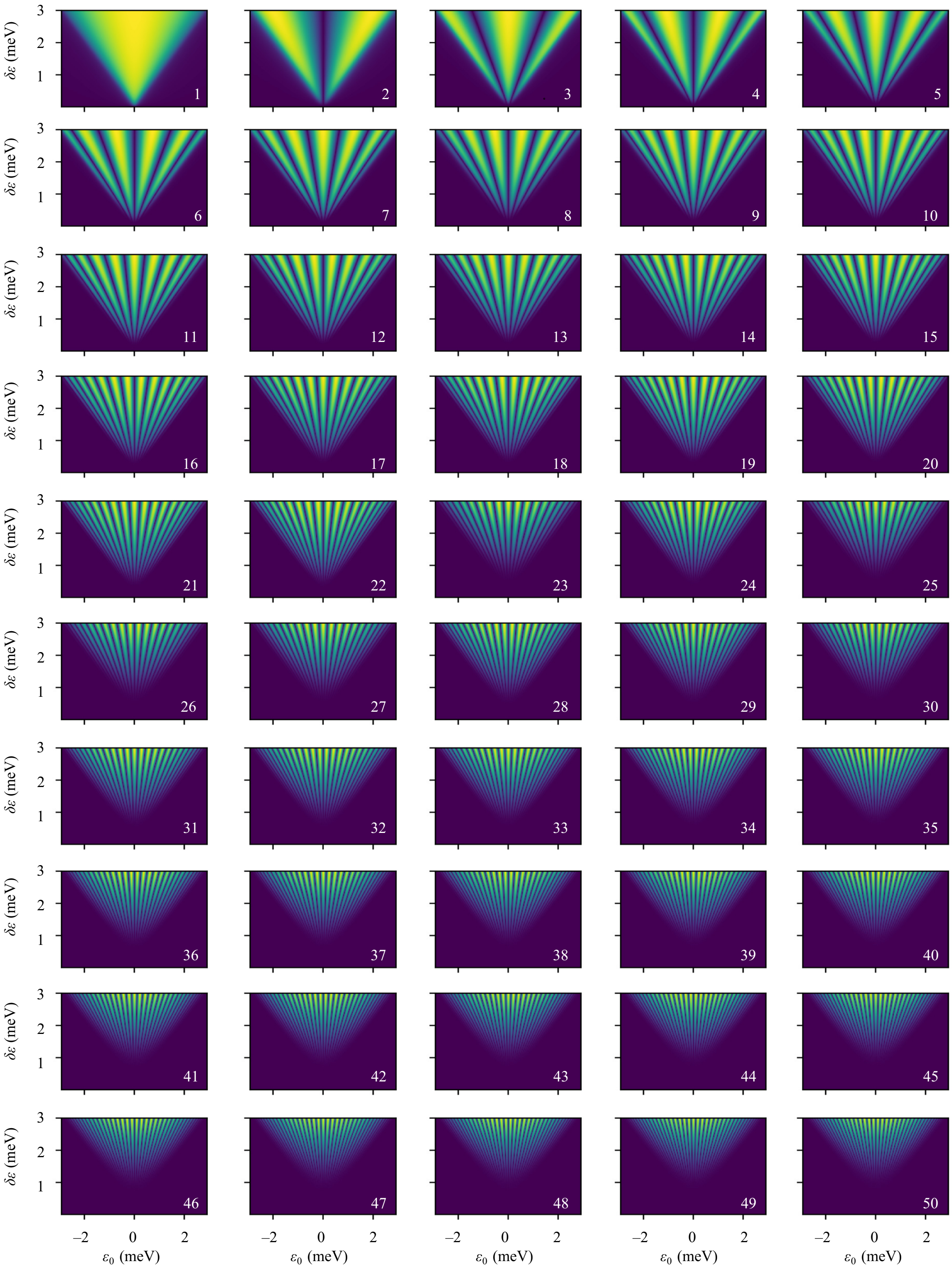

FIG. 15. The simulated data of the first 50 DTR transition harmonics.

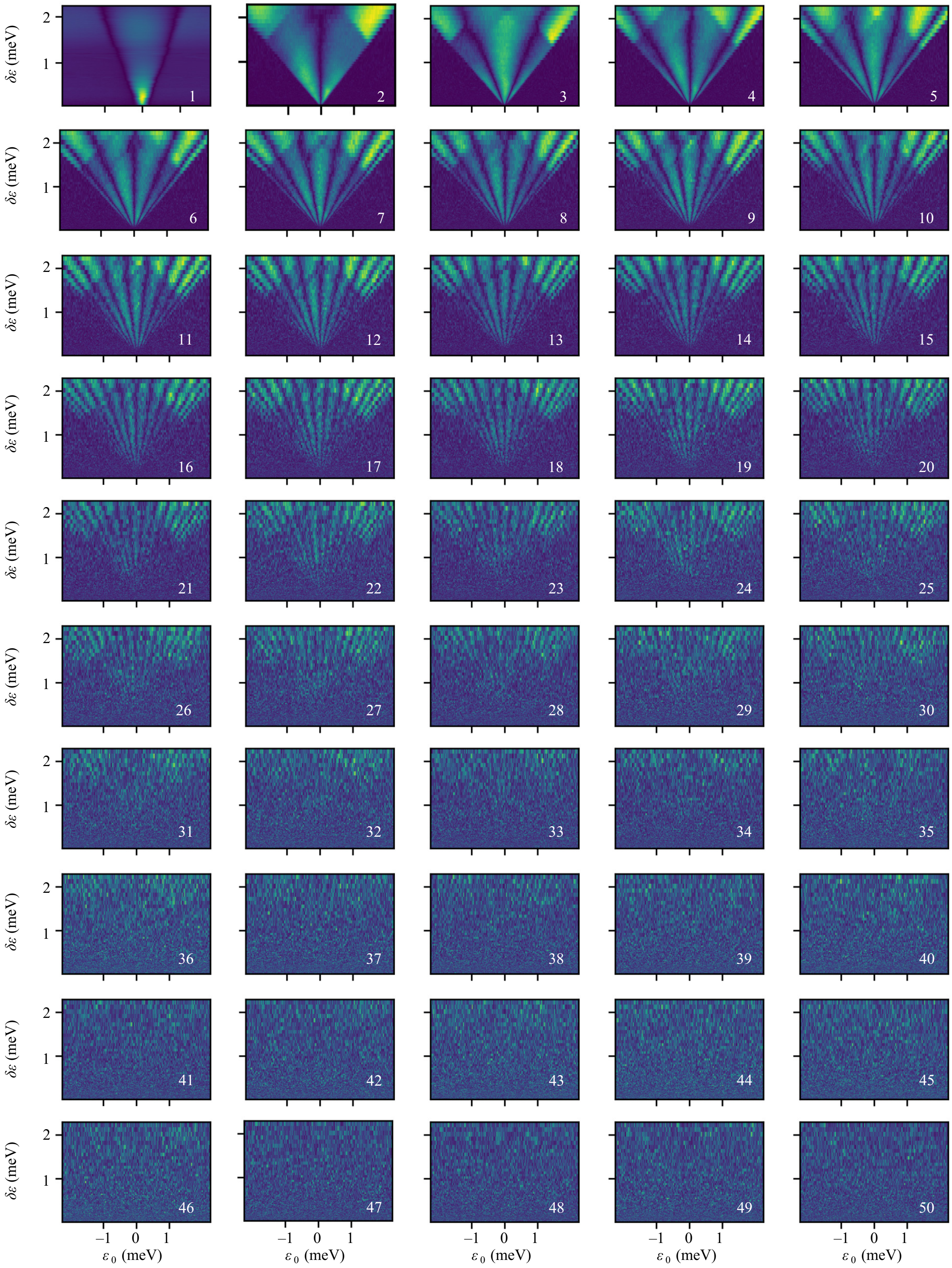

FIG. 16. The raw data of first 50 harmonics experimentally measured across an ICT.

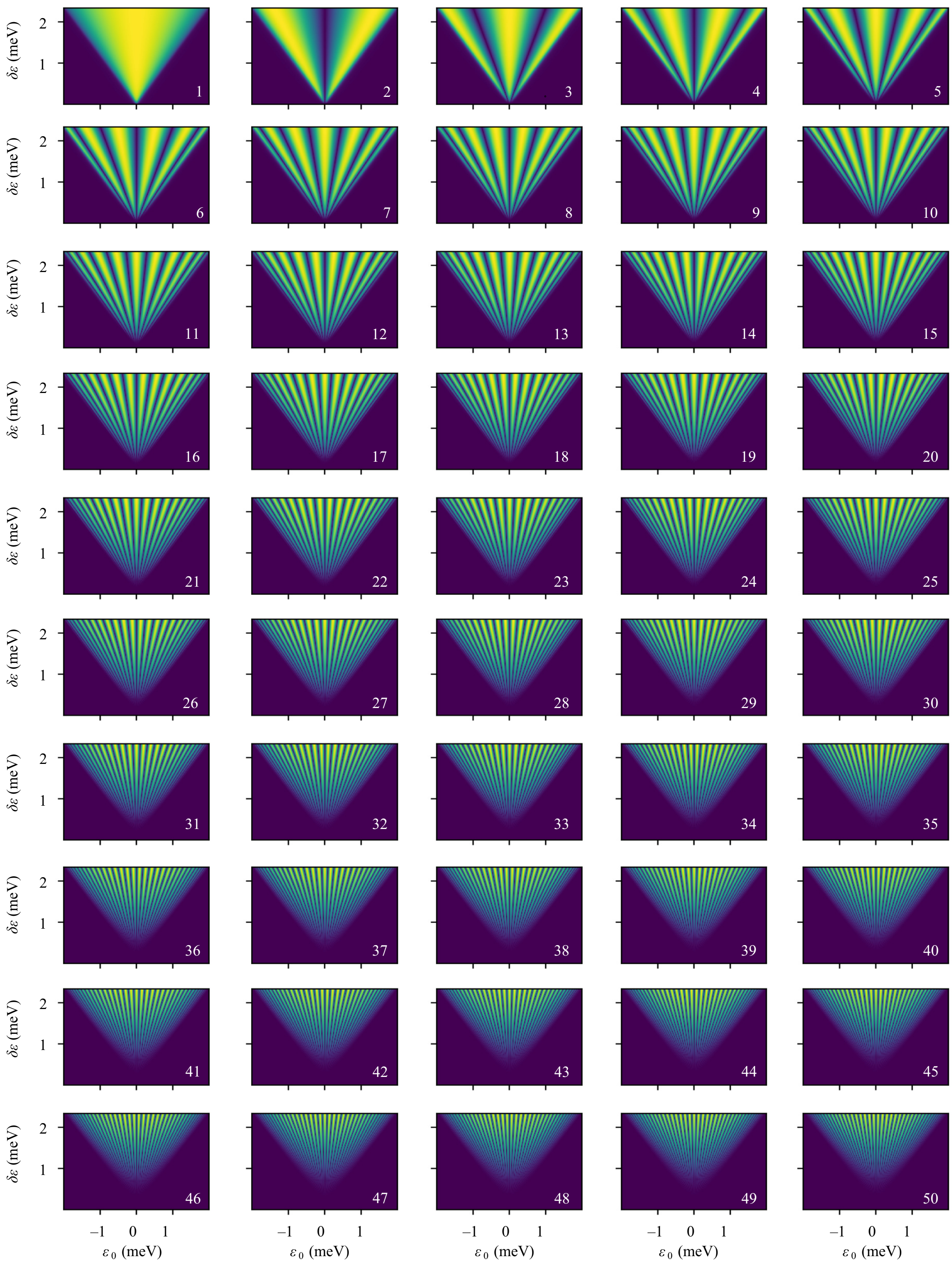

FIG. 17. The simulated data of the first 50 ICT harmonics.

In this limit, this process is essentially equivalent to *shot* noise [36,52]. Typical of a Poisson process, in this case, we have

$$S_I \approx \alpha_c e \frac{\pi}{2} N |I_N|, \tag{N5}$$

which shows how the signal becomes comparable with the intrinsic noise. Considering the power SNR_I, we have

$$\mathrm{SNR}_I = \frac{2|I_N|}{N\pi\alpha_c e \Delta\omega_r} \approx \frac{2}{\pi^2}\frac{Q_r}{N^3}\frac{\Gamma_R}{\omega_0}. \tag{N6}$$

Comparing Eqs. (N2) and (N6)—in particular, the ratio Γ_R/ω_0—it ought to be clear that the shot-noise regime is undesirable for the operation of the DTR transition as a frequency multiplier. Interestingly, the transition between jitter noise and charge noise only depends on the ratio between Γ_R and the *driving* frequency ω_0 and SNR_I has the same dependence on the multiplication factor N. Moreover, for increasing ω_r, the spectrum of the intrinsic noise generated by the multiplier becomes increasingly white.

Finally, in the case of the DQD, we stress how the coherent tunneling is formally free of any stochastic component. Thus, intrinsic noise only arises from the jump operators in the LME.

APPENDIX O: HARMONIC REJECTION

Harmonic rejection has been measured through the spectrum analyzer for the case of the DTR. We stress that this is primarily a property of the band-pass filter rather than the quantum system used for harmonic generation. In our case, the resonator has a bandwidth of 5 MHz (for a complete characterization of the resonator in this setup, see Ref. [20]), which is much larger than the difference in frequency between the different N. Therefore, driving the DTR at frequency ω_r/N_D and measuring at frequency ω_r/N_M, the other potentially detectable harmonics are those where N_D is a multiple of N_M. Table I summarizes this measurement for the first $N_D \in [1, 10]$.

We see how the large quality factor of our band-pass filter allows for a rejection of the fundamental ($N_D = N_M$) larger than −68 dBc, while all other spurious signals remain below −60 dBc. The sharpness of the band-pass filter comes at the expense of the tunability of the frequency without tuning the filter itself. Thus, it ought to be engineered according to the specific use case.

APPENDIX P: DTR TRANSITION HARMONICS

In this appendix, we present measurements and simulations of the DTR transition harmonics from $N = 1$ to $N = 50$ (see Figs. 14 and 15, respectively).

APPENDIX Q: ICT HARMONICS

In this appendix, we present measurements and simulations of the ICT harmonics from $N = 1$ to $N = 50$ (see Figs. 16 and 17, respectively).

[1] D. Loss and D. P. DiVincenzo, Quantum computation with quantum dots, Phys. Rev. A **57**, 120 (1998).

[2] N. W. Hendrickx, W. I. Lawrie, M. Russ, F. van Riggelen, S. L. de Snoo, R. N. Schouten, A. Sammak, G. Scappucci, and M. Veldhorst, A four-qubit germanium quantum processor, Nature **591**, 580 (2021).

[3] S. G. J. Philips, M. T. Mądzik, S. V. Amitonov, S. L. de Snoo, M. Russ, N. Kalhor, C. Volk, W. I. L. Lawrie, D. Brousse, L. Tryputen, B. P. Wuetz, A. Sammak, M. Veldhorst, G. Scappucci, and L. M. K. Vandersypen, Universal control of a six-qubit quantum processor in silicon, Nature **609**, 919 (2022).

[4] F. Borsoi, N. W. Hendrickx, V. John, S. Motz, F. van Riggelen, A. Sammak, S. L. de Snoo, G. Scappucci, and M. Veldhorst, Shared control of a 16 semiconductor quantum dot crossbar array, arXiv preprint arXiv:2209.06609 (2022).

[5] X. Xue, M. Russ, N. Samkharadze, B. Undseth, A. Sammak, G. Scappucci, and L. M. Vandersypen, Quantum logic with spin qubits crossing the surface code threshold, Nature **601**, 343 (2022).

[6] A. Noiri, K. Takeda, T. Nakajima, T. Kobayashi, A. Sammak, G. Scappucci, and S. Tarucha, Fast universal quantum gate above the fault-tolerance threshold in silicon, Nature **601**, 338 (2022).

[7] A. R. Mills, C. R. Guinn, M. J. Gullans, A. J. Sigillito, M. M. Feldman, E. Nielsen, and J. R. Petta, Two-qubit silicon quantum processor with operation fidelity exceeding 99%, Sci. Adv. **8**, eabn5130 (2022).

[8] R. Maurand, X. Jehl, D. Kotekar-Patil, A. Corna, H. Bohuslavskyi, R. Laviéville, L. Hutin, S. Barraud, M. Vinet, M. Sanquer, and S. De Franceschi, A CMOS silicon spin qubit, Nat. Commun. **7**, 13575 (2016).

[9] A. M. J. Zwerver, T. Krähenmann, T. F. Watson, L. Lampert, H. C. George, R. Pillarisetty, S. A. Bojarski, P. Amin, S. V. Amitonov, J. M. Boter *et al.*, Qubits made by advanced semiconductor manufacturing, Nat. Electron. **5**, 184 (2022).

[10] E. Charbon, F. Sebastiano, A. Vladimirescu, H. Homulle, S. Visser, L. Song, and R. M. Incandela, in *2016 IEEE International Electron Devices Meeting (IEDM)* (IEEE, San Francisco, CA, 2016), p. 13.5.1.

[11] X. Xue, B. Patra, J. P. G. van Dijk, N. Samkharadze, S. Subramanian, A. Corna, B. P. Wuetz, C. Jeon, F. Sheikh, E. Juarez-Hernandez *et al.*, CMOS-based cryogenic control of silicon quantum circuits, Nature **593**, 205 (2021).

[12] A. Ruffino, T.-Y. Yang, J. Michniewicz, Y. Peng, E. Charbon, and M. F. Gonzalez-Zalba, A cryo-CMOS chip that integrates silicon quantum dots and multiplexed dispersive readout electronics, Nat. Electron. **5**, 53 (2022).

[13] R. Li, L. Petit, D. P. Franke, J. P. Dehollain, J. Helsen, M. Steudtner, N. K. Thomas, Z. R. Yoscovits, K. J. Singh, S.

Wehner, *et al.*, A crossbar network for silicon quantum dot qubits, Sci. Adv. **4**, eaar3960 (2018).

[14] M. Veldhorst, H. Eenink, C.-H. Yang, and A. S. Dzurak, Silicon CMOS architecture for a spin-based quantum computer, Nat. Commun. **8**, 1 (2017).

[15] L. Vandersypen, H. Bluhm, J. Clarke, A. Dzurak, R. Ishihara, A. Morello, D. Reilly, L. Schreiber, and M. Veldhorst, Interfacing spin qubits in quantum dots and donors—hot, dense, and coherent, npj Quantum Inf. **3**, 1 (2017).

[16] M. Gonzalez-Zalba, S. de Franceschi, E. Charbon, T. Meunier, M. Vinet, and A. Dzurak, Scaling silicon-based quantum computing using CMOS technology, Nat. Electron. **4**, 872 (2021).

[17] J. M. Boter, J. P. Dehollain, J. P. G. van Dijk, Y. Xu, T. Hensgens, R. Versluis, H. W. L. Naus, J. S. Clarke, M. Veldhorst, F. Sebastiano, and L. M. K. Vandersypen, Spiderweb Array: A Sparse Spin-Qubit Array, Phys. Rev. Appl. **18**, 024053 (2022).

[18] O. Crawford, J. Cruise, N. Mertig, and M. Gonzalez-Zalba, Compilation and scaling strategies for a silicon quantum processor with sparse two-dimensional connectivity, npj Quantum Inf. **9**, 13 (2023).

[19] M. A. Fogarty, arXiv preprint arXiv:2208.09172 (2022).

[20] G. A. Oakes, V. N. Ciriano-Tejel, D. F. Wise, M. A. Fogarty, T. Lundberg, C. Lainé, S. Schaal, F. Martins, D. J. Ibberson, L. Hutin, *et al.*, Fast High-Fidelity Single-Shot Readout of Spins in Silicon Using a Single-Electron Box, Phys. Rev. X **13**, 011023 (2023).

[21] D. J. Niegemann, V. El-Homsy, B. Jadot, M. Nurizzo, B. Cardoso-Paz, E. Chanrion, M. Dartiailh, B. Klemt, V. Thiney, C. Bäuerle, P.-A. Mortemousque, B. Bertrand, H. Niebojewski, M. Vinet, F. Balestro, T. Meunier, and M. Urdampilleta, Parity and singlet-triplet high fidelity readout in a silicon double quantum dot at 0.5 k (2022).

[22] I. Ahmed, A. Chatterjee, S. Barraud, J. J. Morton, J. A. Haigh, and M. F. Gonzalez-Zalba, Primary thermometry of a single reservoir using cyclic electron tunneling to a quantum dot, Commun. Phys. **1**, 1 (2018).

[23] J. M. A. Chawner, S. Barraud, M. F. Gonzalez-Zalba, S. Holt, E. A. Laird, Y. A. Pashkin, and J. R. Prance, Nongalvanic Calibration and Operation of a Quantum Dot Thermometer, Phys. Rev. Appl. **15**, 034044 (2021).

[24] L. Cochrane, T. Lundberg, D. J. Ibberson, L. A. Ibberson, L. Hutin, B. Bertrand, N. Stelmashenko, J. W. A. Robinson, M. Vinet, A. A. Seshia, and M. F. Gonzalez-Zalba, Parametric Amplifiers Based on Quantum Dots, Phys. Rev. Lett. **128**, 197701 (2022).

[25] C. T.-c. Nguyen, MEMS technology for timing and frequency control, IEEE Trans. Ultrason. Ferroelectr. Freq. Control **54**, 251 (2007).

[26] D. J. Ibberson, L. Bourdet, J. C. Abadillo-Uriel, I. Ahmed, S. Barraud, M. J. Calderón, Y.-M. Niquet, and M. F. Gonzalez-Zalba, Electric-field tuning of the valley splitting in silicon corner dots, Appl. Phys. Lett. **113**, 53104 (2018).

[27] K. Petersson, C. Smith, D. Anderson, P. Atkinson, G. Jones, and D. Ritchie, Charge and Spin State Readout of a Double Quantum Dot Coupled to a Resonator, Nano Lett. **10**, 2789 (2010).

[28] C. Ciccarelli and A. J. Ferguson, Impedance of the single-electron transistor at radio-frequencies, New J. Phys. **13**, 093015 (2011).

[29] S. J. Chorley, J. Wabnig, Z. V. Penfold-Fitch, K. D. Petersson, J. Frake, C. G. Smith, and M. R. Buitelaar, Measuring the Complex Admittance of a Carbon Nanotube Double Quantum Dot, Phys. Rev. Lett. **108**, 036802 (2012).

[30] R. Mizuta, R. M. Otxoa, A. C. Betz, and M. F. Gonzalez-Zalba, Quantum and tunneling capacitance in charge and spin qubits, Phys. Rev. B **95**, 045414 (2017).

[31] M. Esterli, R. Otxoa, and M. Gonzalez-Zalba, Small-signal equivalent circuit for double quantum dots at low-frequencies, Appl. Phys. Lett. **114**, 253505 (2019).

[32] V. D. Maman, M. F. Gonzalez-Zalba, and A. Pályi, Charge Noise and Overdrive Errors in Dispersive Readout of Charge, Spin, and Majorana Qubits, Phys. Rev. Appl. **14**, 064024 (2020).

[33] D. Manzano, A short introduction to the Lindblad master equation, AIP Adv. **10**, 025106 (2020).

[34] T. H. Lee and A. Hajimiri, Oscillator phase noise: A tutorial, IEEE J. Solid-State Circuits **35**, 326 (2000).

[35] L. Cochrane, A. A. Seshia, and M. F. G. Zalba, Intrinsic noise of the single electron box (2022).

[36] F. D. Parmentier, E. Bocquillon, J. M. Berroir, D. C. Glattli, B. Plaçais, G. Fève, M. Albert, C. Flindt, and M. Büttiker, Current noise spectrum of a single-particle emitter: Theory and experiment, Phys. Rev. B **85**, 165438 (2012).

[37] N. Dittmann and J. Splettstoesser, Finite-frequency noise of interacting single-electron emitters: Spectroscopy with higher noise harmonics, Phys. Rev. B **98**, 115414 (2018).

[38] M. Moskalets, Noise of a single-electron emitter, Phys. Rev. B **88**, 035433 (2013).

[39] F. Vigneau, F. Fedele, A. Chatterjee, D. Reilly, F. Kuemmeth, F. Gonzalez-Zalba, E. Laird, and N. Ares, Probing quantum devices with radio-frequency reflectometry (2022).

[40] C. X. Yu, S. Zihlmann, J. C. Abadillo-Uriel, V. P. Michal, N. Rambal, H. Niebojewski, T. Bedecarrats, M. Vinet, É. Dumur, M. Filippone, B. Bertrand, S. De Franceschi, Y.-M. Niquet, and R. Maurand, Strong coupling between a photon and a hole spin in silicon, Nat. Nanotechnol., 1 (2023).

[41] X. Croot, X. Mi, S. Putz, M. Benito, F. Borjans, G. Burkard, and J. R. Petta, Flopping-mode electric dipole spin resonance, Phys. Rev. Res. **2**, 012006 (2020).

[42] J. I. Colless, A. C. Mahoney, J. M. Hornibrook, A. C. Doherty, H. Lu, A. C. Gossard, and D. J. Reilly, Dispersive Readout of a Few-Electron Double Quantum Dot with Fast rf Gate Sensors, Phys. Rev. Lett. **110**, 046805 (2013).

[43] M. F. Gonzalez-Zalba, S. Barraud, A. J. Ferguson, and A. C. Betz, Probing the limits of gate-based charge sensing, Nat. Commun. **6**, 6084 (2015).

[44] N. Ares, F. J. Schupp, A. Mavalankar, G. Rogers, J. Griffiths, G. A. C. Jones, I. Farrer, D. A. Ritchie, C. G. Smith, A. Cottet, G. A. D. Briggs, and E. A. Laird, Sensitive Radio-Frequency Measurements of a Quantum Dot by Tuning to Perfect Impedance Matching, Phys. Rev. Appl. **5**, 034011 (2016).

[45] E. Jeffrey, D. Sank, J. Y. Mutus, T. C. White, J. Kelly, R. Barends, Y. Chen, Z. Chen, B. Chiaro, A. Dunsworth, A. Megrant, P. J. J. O'Malley, C. Neill, P. Roushan, A. Vainsencher, J. Wenner, A. N. Cleland, and J. M. Martinis, Fast Accurate State Measurement with Superconducting Qubits, Phys. Rev. Lett. **112**, 190504 (2014).

[46] K. Thirumalaivasan and R. Nakkeeran, Development of Compact Ultra-Wideband (UWB) microstrip bandpass filter, J. Electromagnetic Anal. Appl. **3**, 333 (2011).

[47] A.-L. Franc, E. Pistono, D. Gloria, and P. Ferrari, High-performance shielded coplanar waveguides for the design of CMOS 60-GHz bandpass filters, IEEE Trans. Electron. Devices **59**, 1219 (2012).

[48] S. Shevchenko, S. Ashhab, and F. Nori, Landau-Zener-Stückelberg interferometry, Phys. Rep. **492**, 1 (2010).

[49] J. Duan, M. A. Fogarty, J. Williams, L. Hutin, M. Vinet, and J. J. Morton, Remote capacitive sensing in two-dimensional quantum-dot arrays, Nano Lett. **20**, 7123 (2020).

[50] R. Navid, T. H. Lee, and R. W. Dutton, An analytical formulation of phase noise of signals with Gaussian-distributed jitter, IEEE Trans. Circuits Syst. II: Express Briefs **52**, 149 (2005).

[51] L. Kranz, S. K. Gorman, B. Thorgrimsson, Y. He, D. Keith, J. G. Keizer, and M. Y. Simmons, Exploiting a single-crystal environment to minimize the charge noise on qubits in silicon, Adv. Mater. **32**, 2003361 (2020).

[52] T. Hasler, M. Jung, V. Ranjan, G. Puebla-Hellmann, A. Wallraff, and C. Schonenberger, Shot Noise of a Quantum Dot Measured with Gigahertz Impedance Matching, Phys. Rev. Appl. **4**, 054002 (2015).